AD-769 500

AN INVESTIGATION OF FORCES ON A PRO-
JECTILE DURING PERFORATION OF THIN
ALUMINUM PLATES

Visi Arajs

Air Force Institute of Technology
Wright-Patterson Air Force Base, Ohio

June 1971

DOCUMENT CONTROL DATA - R & D		
(Security classification of title, body of abstract and indexing annotation must be entered when the overall report is classified)		

1. ORIGINATING ACTIVITY (Corporate author)	2a. REPORT SECURITY CLASSIFICATION
Air Force Institute of Technology (AFIT-EN) Wright-Patterson AFB, Ohio 45433	Unclassified
	2b. GROUP

3. REPORT TITLE

AN INVESTIGATION OF FORCES ON A PROJECTILE DURING PERFORATION OF THIN ALUMINUM PLATES

4. DESCRIPTIVE NOTES *(Type of report and inclusive dates)*

AFIT Thesis

5. AUTHOR(S) *(First name, middle initial, last name)*

Visi Arajs, Captain, USAF

6. REPORT DATE	7a. TOTAL NO. OF PAGES	7b. NO. OF REFS
June 1971	98 111	23

8a. CONTRACT OR GRANT NO.	9a. ORIGINATOR'S REPORT NUMBER(S)
N/A	AFIT Thesis
b. PROJECT NO. 7360	GAW/MC/71-3
c. Task N. 736006	9b. OTHER REPORT NO(S) *(Any other numbers that may be assigned this report)*
d.	N/A

10. DISTRIBUTION STATEMENT

Approved for public release; distribution unlimited.

Details of illustrations in this document may be better studied on microfiche.

11. *"Approved for public release; IAW AFR 190-17* JERRY C. HIX, Captain, USAF Director of Information	12. SPONSORING MILITARY ACTIVITY Air Force Materials Laboratory Wright-Patterson AFB, Ohio 45433

13. ABSTRACT

The reverse forces encountered by projectiles during ordnance velocity perforation of thin aluminum plates were determined for four projectile configurations and three plate thicknesses. The investigation was conducted by holding simulated projectiles stationary and impacting them with aluminum plates. Strain gages bonded to the stationary targets were used to obtain a strain versus time record during perforation; this was subsequently converted into a perforation force record by application of strain wave propagation and linear strain theories. The projectile nose configurations investigated included two cones, a hemisphere and a flat ended cylinder. Peak perforation force and projectile efficiency comparisons were made with results from other investigations.
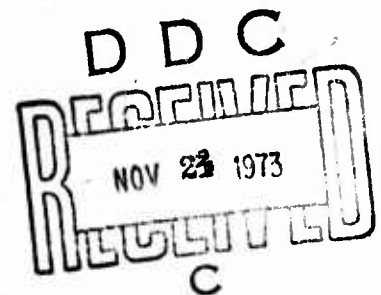
DD FORM 1473 1 NOV 65

14. KEY WORDS	LINK A		LINK B		LINK C	
	ROLE	WT	ROLE	WT	ROLE	WT
1. Perforation Force						
2. Projectile Shape						
3. Thin Plate Perforation						

ia

AN INVESTIGATION OF FORCES ON A
PROJECTILE DURING PERFORATION
OF THIN ALUMINUM PLATES

THESIS

GAW/MC/71-3   Visi Arajs
                     Captain USAF

Approved for public release; distribution unlimited.

i b

AN INVESTIGATION OF FORCES ON A

PROJECTILE DURING PERFORATION

ON THIN ALUMINUM PLATES

THESIS

Presented to the Faculty of the School of Engineering of

the Air Force Institute of Technology

Air University

in Partial Fulfillment of the

Requirements for the Degree of

Master of Science

By

Visi Arajs, B. S. A. E.
Captain   USAF

Graduate Air Weapons

June 1971

Preface

The successful conduct of this investigation required the application of many disciplines in the fields of engineering, physics, and ordnance technology; many more than a single individual could master proficiently in the limited time available. Thus without the outstanding help provided by faculty members of the Air Force Institute of Technology and laboratory personnel at the University of Dayton Research Institute, this report would not have been possible.

Specifically, I wish to thank Major William Goldberg, Mr. Hallock F. Swift, Mr. Diamantis D. Preonas, and Mr. Paul W. Dueweke for their advice in the practical and theoretical aspects of this program. Also a special thank-you is due Mr. Michael Lehman for his gun range and instrumentation design work, and his patient help during the experiments. Similarly a debt of gratitude is owed to Mr. James Green, whose many hours of bonding strain gages contributed significantly to the successful completion of this investigation.

Visi Arajs

Contents

Contents (continued)

<u>Contents</u> (continued)

List of Figures

List of Figures (continued)

List of Tables

ABSTRACT

The impact forces encountered by projectiles during ordnance velocity perforation of thin aluminum plates were determined for four projectile configurations and three plate thicknesses. The investigation was conducted by holding simulated projectiles stationary and impacting them with aluminum plates. Strain gages bonded to the stationary targets were used to obtain a strain versus time record during perforation; this was subsequently converted into a perforation force record by application of strain wave propagation and linear strain theories. The projectile nose configurations investigated included two cones, a hemisphere and a flat ended cylinder. Peak perforation force and projectile efficiency comparisons were made with results from other investigations.

I. Introduction

Recent aircraft losses due to ground fire in Southeast Asia point up the need for more detailed knowledge of the resisting forces a projectile encounters when perforating aircraft skin at ordnance velocities. By use of these forces and the physical characteristics of the projectile, the residual velocity with which the projectile can strike internal aircraft components can be calculated. This in turn can p   le data for design of better protection systems and give additional insight into the perforation process.

Object

The object of this investigation was to determine experimentally the forces that projectiles of simple geometrical shape and traveling at ordnance velocities encounter during perforation of thin aluminum plates. A secondary objective was to compare the results of this program with those of several other experimental studies of a similar nature. The comparisons are limited to specific areas defined later in this report.

Although the perforation of aluminum plates can occur at many angles of projectile incidence and over a large range of velocities, this experimental study was specifically limited to measuring the impact force versus time history on projectiles during normal incidence perforation at velocities in the range of 500 meters per second. This investigation was further limited to measuring such forces on projectiles with conical, hemispherical, and cylindrical nose shapes which were targeted

against three thicknesses of aluminum plates.

Definitions

A number of definitions are adhered to in this report. Perforation is taken to mean complete passage of the projectile through the target material; and ordnance velocity is seen as the velocity a projectile must have, just before impact, to perforate the skin of an aircraft and cause unacceptable damage to internal components. Such a velocity can be imparted to a projectile by many of a vast variety of antiaircraft weapons.

Factors

This study was conducted by use of a technique pioneered in 1954 by Mr. Joseph I. Bluhm of the Watertown Arsenal Laboratories (Ref 2). The usual method of investigation was reversed in that the "projectile" was held stationary, and the target plate fired at it. This technique allows the indirect measurement of perforation forces by means of strain gages bonded to the simulated projectile, and thus overcomes the usual difficulty of instrumenting a projectile moving at high velocity. A more detailed discussion of this technique follows later in the report.

Background

Projectile perforation of thin metal plates occurs when the plate fails in one or more modes upon projectile impact. These modes can generally be categorized as plugging, petaling, or a combination of both (Ref 5). They can also be accompanied by phenomena such as friction

heating, spallation and clastic and plastic wave propagation (Ref 9:24).
Petaling and plugging failures are illustrated in Fig. 1.

Petaling occurs when stresses induced by the initial impact of the
projectile form cracks in the plate radially outward from the point of im-
pact. The plate material then fails and petals back to allow projectile
passage (Ref 19). Plugging takes place when the projectile shears or
tears out a section of the plate of approximately equal diameter to that
of the projectile (Ref 19).

A number of theories have been proposed by various authors to
explain these perforation mechanisms, and most of these concentrate on
approximating the velocity a projectile will have after perforation by use
of energy principles. On the other hand, the examination of forces
encountered by a projectile during perforation has been the object of
several experiments. Some of these are discussed in the next section.
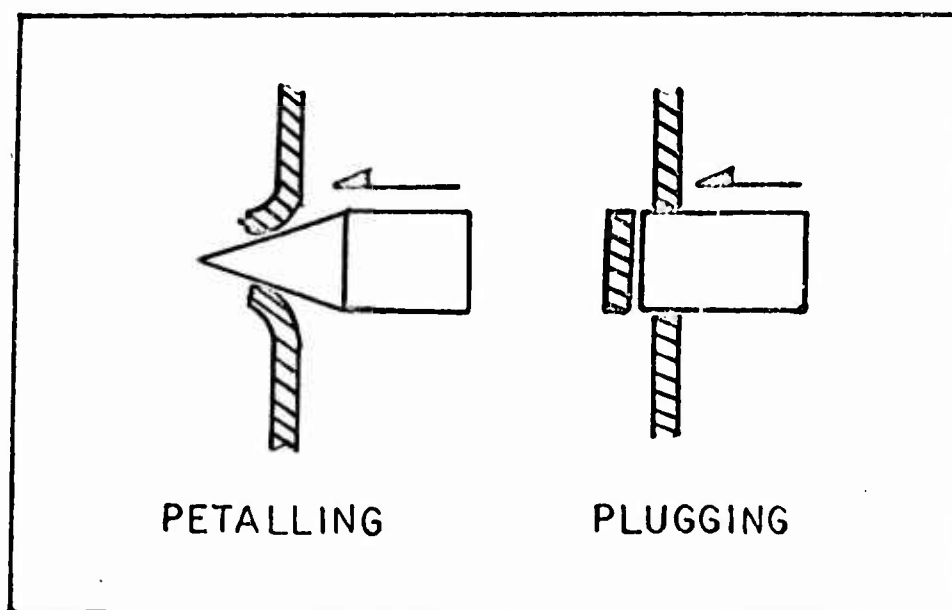
Fig. 1. Thin Plate Perforation Failure Modes

Prior Work in the Field of Perforation Mechanics and Stress Wave Propagation

Guidelines for the conduct of this investigation were based upon data and techniques developed during similar research projects in the past. The measurement of forces resisting projectile perforation first received detailed attention during World War II, but these efforts were hampered by lack of accurate instrumentation (Ref 13). It was not until 1948 that Mr. A. V. Masket of the Naval Research Laboratory succeeded in obtaining meaningful data in this area (Ref 13). He used an early form of streak camera to obtain a shadow photographic record of projectile motion during perforation of steel armor plates. This technique allowed the measurement of the position and velocity of the trailing edge of the projectile during perforation at intervals of .5 microsecond. From this data, Masket calculated the resisting force versus time record.

This experiment yielded a number of significant items which were used by later researchers. These included an accurate measurement of perforation times for various armor thicknesses, and the determination that short time perforation forces induce longitudinal oscillations in the projectile. It was also learned that, for normal incidence impact, transverse vibrations of the projectile are negligible. Of further significance was the discovery that projectile decelerations as high as 1.5 megagees were possible during perforation.

A more direct method of obtaining perforation force versus time data was mentioned earlier as having been introduced by Bluhm (Ref 2),

and a modified form of his technique was used to gather data for this report. In the Bluhm experiments, the plate to be perforated was fired at a stationary object configured as a projectile and instrumented with resistance wire strain gages. Bluhm bonded one strain gage on each side of his "projectile" so that each could respond to longitudinally sweeping strain pulses induced by the perforation process. This assembly was then mounted in front of a 37-millimeter gun muzzle by means of a wood and cardboard support frame. The plate was soldered to the open end of a hollowed out 37-millimeter projectile, and fired at the stationary target. Data was collected by photographing oscilloscope traces produced by the strain gage circuit during perforation. The resulting strain versus time record was presented with no attempt to convert strain readings to force readings, though this could have been done readily by use of stress-strain relationships for the target material. Normal incidence perforation was investigated first (Ref 2), and oblique perforation experiments were conducted later by reorienting the experimental layout (Ref 3).

Bluhm points out both the advantages and disadvantages of this technique. A major advantage is that this method eliminates the difficult task of instrumenting a high speed projectile. An important disadvantage is that this system does not fully simulate a real-life situation Normally a projectile is subject to forces prior to its impact with the plate, but in this procedure, the plate is subject to these forces while the projectile is not. Further, stress waves propagated radially

outward from the point of perforation in a 37-millimeter plate can reflect at the edge and return to influence the impact process before it is completed.

More recent investigations in the area of perforation mechanics have been conducted by Major Thomas E. Fields (Ref 5) and Captain Richard D. Gabbert (Ref 6) of the Air Force Institute of Technology. Both individuals investigated projectile velocity loss after perforation of aluminum plates as a function of projectile nose shape. Neither made an attempt to measure projectile-resisting forces during the dynamic phase of their experimental programs; however, Gabbert did perform resisting force versus displacement measurements-for a number of projectile shapes under quasistatic perforation conditions. These measurements were carried out by slowly forcing a projectile through an aluminum plate with a compression testing machine and measuring the force displacement profile required to do so. Fields and Gabbert reached conclusions concerning the relative perforation efficiency of various projectile shapes.

The work of Fields and Gabbert has been mentioned because a secondary objective of this investigation is to compare the peak forces obtained by Gabbert in his slow perforation experiment with those derived from this study for the same projectile shapes and plate thicknesses. Further, the conclusions reached by Fields concerning perforation efficiency will be compared with those reached from the data of this study.

Since the accuracy of data gathered in this program depends

upon the characteristics of stress wave propagation in bounded media,
the main points of several past investigations in this area are reviewed
here. Cunningham and Goldsmith (Ref 4) measured strain pulses in long
rectangular aluminum and steel bars resulting from the longitudinal
impact of small steel spheres on one end. Both crystal tranducers and
strain gages bonded to the bars were used to gather data. In addition,
the bar was suspended as a ballistic pendulum whose displacement was
measured subsequent to each impact. A uniform stress distribution
across the bars was assumed, and impact force versus time curves were
calculated from the strain data.

Another experimental program dealing with stress wave propagation
in truncated cones was conducted by Goldsmith (Ref 8). In this investi-
gation, cones with apex angles of .48, 5.38, 20, and 30 degrees were
impacted by small steel balls either at their base or apex ends. The
resulting strain pulses were recorded by a series of strain gages located
at intervals along the length of the cones. Goldsmith was primarily
interested in strain pulse distortion as a function of the distance traveled
in the cone. His results are discussed in Chapter V of this report.

Purpose

The purpose of this report is to generate and present experimental
data concerning the forces encountered by projectiles during ordnance
velocity perforation of thin aluminum plates. The resultant perforation
force versus time records will be examined to see how they vary with

projectile nose shape and plate thickness, and comparisons will be made with the peak force data obtained by Gabbert. In addition, estimates of projectile perforation efficiency will be made by measuring areas under the perforation force versus time curves for each projectile configuration tested, and by calculating the resultant velocity loss on projectiles fired by both Fields and Gabbert. The conclusions concerning perforation efficiency will be compared with those reached by Fields for the same projectile shapes.

Report Organization

The subsequent sections of this report present a general description of the experimental program, detailed descriptions of the experimental apparatus and procedures, an analysis of possible errors in the data presented, the experimental data and comparisons and the conclusions and recommendations. The appendices contain sample calculations, derivations and the experimental data in raw form.

II. Theoretical Considerations

Theory

It is apparent from the discussion in Chapter I that forces encountered during perforation can be frictional, inertial, shear, compressional or a combination of all four; and that their precise relationship and magnitude as a function of time is difficult to predict analytically. Hence, as mentioned earlier, a number of authors approach the problem from an energy standpoint.

Both Thompson (Ref 23) and Nishiwaki (Ref 14) consider the energy dissipated by the projectile in displacing target material sufficiently to force a passage through the plate. Nishiwaki also considers friction encountered by the projectile during perforation. Both of these theories have been shown to be in error by Fields (Ref 5) in that they predict lower velocity losses than obtained experimentally.

Neither Thompson nor Nishiwaki attempt to predict forces encountered by the projectile as a function of velocity and perforation time. However, a simplified mathematical analysis of the perforation process in terms of those two quantities and the material properties is possible.

Assume that all of the forces acting on a projectile during perforation at a velocity v can be resolved into a single force F(t), acting on the area of contact between target and projectile. Further if it is assumed that all retarding forces are uniformally distributed around the perforation hole, and if the projectile is symmetric about its longitudinal

axis, then the resultant force may be considered as passing through the projectile center of mass. This condition is depicted in Fig. 2.

Now let m be the mass of the projectile, and v(t) its time varying velocity during perforation, then

$$F(t) = -m\frac{dv}{dt} \qquad (1)$$

It is often assumed that resistance to projectile motion through a fluid medium is proportional to some power of the projectile velocity (Ref 15:304). Hence it does not seem unreasonable to assume that forces resisting perforation are also functions of perforation velocity raised to a power; particularly if the target material is softer than the projectile material
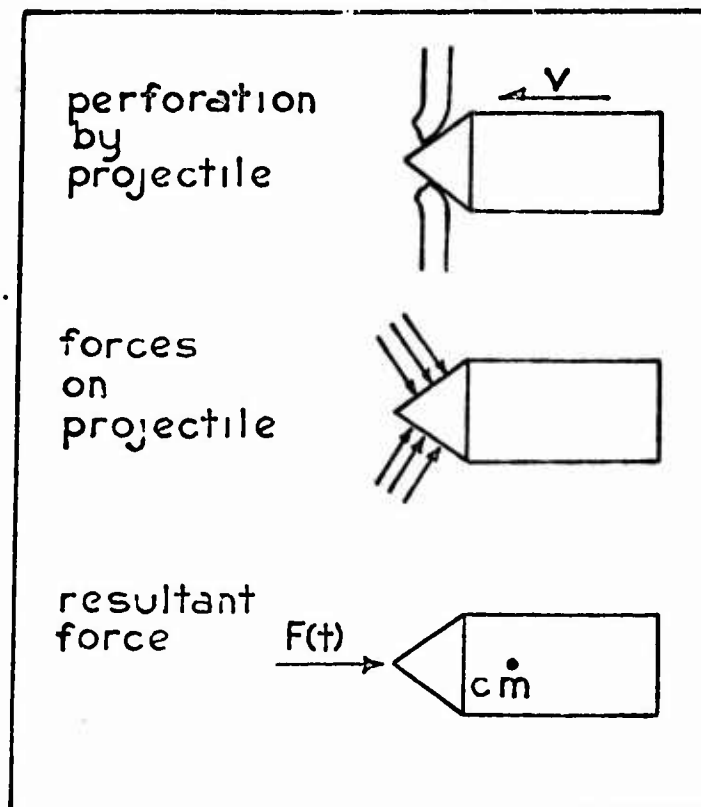
Fig. 2. A Perforation Force Model

and the projectile does not deform. Then let

$$F(t) = K \left[\frac{v}{v_*} \right]^n$$

(2)

Where K is a proportionality constant with units of force, n is some positive real number and v_* is a factor to normalize v. Now substituting Equation 2 into 1, we get

$$K \left[\frac{v}{v_*} \right]^n = -m \frac{dv}{dt}$$

(3)

or

$$\left[\frac{v}{v_*} \right]^{-n} dv = -\frac{K}{m} dt$$

(4)

Let v_0 and t_0 be the projectile velocity and time just before projectile impact. Similarly let v_f and t_f be the same parameters immediately after perforation is completed. Then

$$\left[v_0 - v_f \right] = \Delta v$$

(5)

will be the velocity loss during perforation, and

$$\left[t_f - t_0 \right] = t_p$$

(6)

will be the perforation time. Integrating both sides of Equation 4, we get for $n \neq 1$

$$\int_{v_0}^{v_f} \frac{dv}{v^n} = -\frac{K}{mv_*^n} \int_{t_0}^{t_f} dt$$

(7)

$$v_f^{(1-n)} - v_0^{(1-n)} = -\frac{K}{mv_*^n} \left[t_f - t_0 \right] \left[1 - n \right]$$

(8)

11

from Equation 6,

$$v_f^{(1-n)} - v_0^{(1-n)} = -\frac{K}{mv_*^n}\left[1-n\right]t_p \tag{9}$$

If n is a positive real number, Equation 9 has two possible forms; one each for $0 < n < 1$ and $n > 1$.

If $0 < n < 1$, then Equation 9 can be rearranged to give

$$v_f^{(1-n)} = v_0^{(1-n)} - \frac{K}{mv_*^n}\left[1-n\right]t_p \tag{10}$$

Equation 10 is valid as long as $v_f^{(1-n)} \geq 0$, and this is true only for perforation times given by

$$t_p \leq \frac{mv_*^n v_0^{(1-n)}}{K\left[1-n\right]} \tag{11}$$

Now if $n > 1$, then $(1-n) < 0$, and Equation 9 becomes

$$v_f = \frac{v_0}{\left[1+\frac{Kv_0^{[n-1]}}{mv_*^n}\left[n-1\right]t_p\right]^{[n-1]}} \tag{12}$$

Equations 10 and 12 are relationships expressing velocity after perforation as a function of perforation time and impact velocity, and they provide a mathematical insight into the perforation process. Equation 10 is consistent with physical expectations since for given values of v_o, n, and K and for t_p limited as in Equation 11, an increase in t_p will cause a decrease in v_f. Equation 12, which is valid for all values of t_p predicts similar results. Further if n increases as target hardness or density increase, both equations give a corresponding decrease in the final perforation velocity.

12

Now for the special case when $n = 1$,

$$F(t) = K\left[\frac{v}{v_*}\right] \tag{13}$$

then

$$\frac{K}{v_*} v = -m\frac{dv}{dt} \tag{14}$$

or

$$\frac{dv}{v} = -\frac{K}{mv_*}dt \tag{15}$$

Again integrating both sides from the initial to the final conditions of perforation

$$\ln v_f - \ln v_o = -\frac{K}{mv_*}(t_f - t_o) \tag{16}$$

or

$$\frac{v_f}{v_o} = \exp\left[-\frac{K}{mv_*}t_p\right] \tag{17}$$

Now since the quantity K/mv_* is positive, Equation 17 predicts a decrease in v_f with an increase in t_p for given values of v_o.

In the results section of this report, approximate values of K and t_p are obtained from the experimental data and used to calculate values of v_f/v_o for one projectile shape by means of Equation 17. This value is then compared with experimental values obtained by Gabbert for the same projectile shape.

Remarks on Stress Waves Generated by Impact and Perforation

Since the data presented in this report was collected by measuring stress waves generated by the perforation process, some remarks about stress wave propagation in bounded media are in order.

Assume that a long slender rod of circular cross section and

moving at some velocity suddenly impacts a rigid object. The stress developed at the impacting end will travel down the bar as a compression pulse. The wave will not be distorted if the bar diameter is small compared to the length of the pulse (Ref 11:88). Then as is shown by the following development, the stress distribution in this pulse can be considered to act over a plane area after some distance of travel in the bar.

A stress disturbance at a point in a continuous medium will travel radially outward with a spherical wave front (Ref 17). If the distrubance point is on the end of a long slender rod, the spherical wave front will propagate along the rod as shown in Fig. 3. Here the dotted extension of the wave indicates its shape if the rod medium was extended outward.

Initially, the spherical wave front will have a velocity component in the direction of the rod surface, and this will result in some fraction of the wave reflecting in tension from the surface (Ref 17). However if the cross sectional area of the rod is small compared to its total length, then the wave front will become approximately planar after traveling a distance
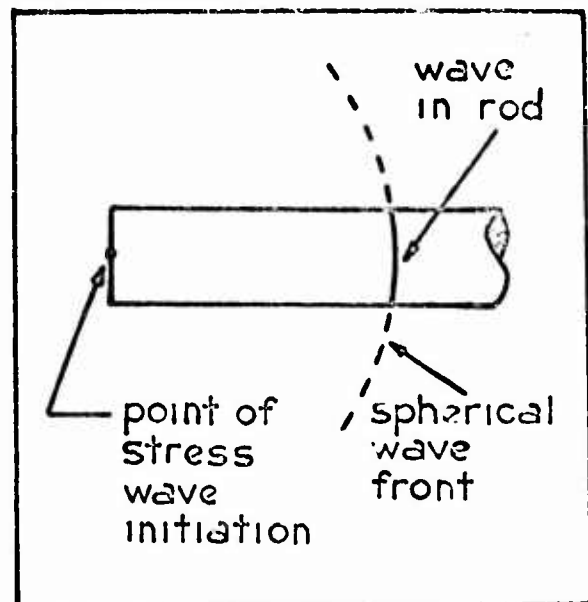
Fig. 3. Wave Propagation in a
Long Slender Rod

equal to several diameters of the rod as is shown clearly in Fig. 3.

If there are an infinite number of disturbance points, such as over the entire end area of a long slender rod, then an infinite number of waves will travel along the rod. Fig. 4 depicts wave initiation at two points on the end of such a rod, and the corresponding state of each at some distance from its point of initiation. If Huygen's Principle (Ref 18:234) is now applied

to this condition, the result will be a new spherical wave front tangent to the surfaces of the two original waves. At some distance from the points of initiation, this spherical wave front can also be approximated by a plane surface. The extension of this concept to an infinite number of initiating points is obvious.
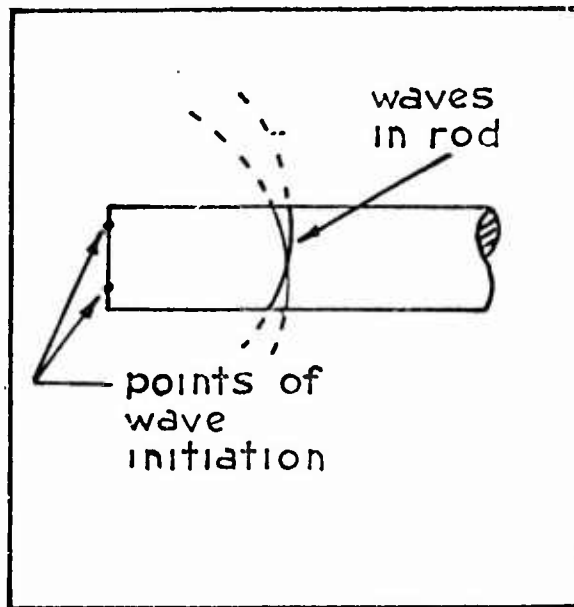
Fig. 4. The Propagation of Two Wave Fronts in a Long Slender Rod

Now if a uniform one-dimensional strain distribution is assumed over the surface of a plane stress wave traveling in a slender circular rod, then the relation between stress and strain over the wave is given by (Ref 11:42)

$$\sigma = E \epsilon \tag{18}$$

15

Where σ is the stress distribution over the wave front, E is the elastic modulus of the material and ϵ is the amplitude of the strain wave. From linear stress-strain theory, this relationship will hold only if the elastic limit of the rod material is not exceeded. If the cross sectional area of the rod at the strain wave is designated by A, then the force represented by the wave is given by

$$F = A\sigma \tag{19}$$

or

$$F = AE\epsilon \tag{20}$$

If there is no energy loss and distortion in the strain wave as it travels along the rod, then F represents the force which caused the wave.

III.   The Experimental Program

The basic experimental program from which data in this report was obtained consisted of firing 38-millimeter diameter aluminum plates bonded to a plastic sabot at a series of stationary 20.32 centimeter long and .95 centimeter diameter steel rods.   The rods differed in end geometry, and were instrumented with strain gages.   A detailed description of the experimental apparatus and procedures is presented in Chapter IV of this report.

Each of four separate rod end configurations was targeted against three plates; .476, .318, and .159 centimeters thick.   The rod end confi urations consisted of cones with 30° and 90° total included apex angles, a .952 cm diameter hemisphere and a flat end.   Each of these configurations is depicted in Fig. 10 of Chapter IV.   In addition, a number of shots were conducted whose main purpose was to obtain a visual record of the perforation process by means of x-ray photography.

The experimental program consisted of 32 shots, of which 5 were partial failures and two were fired to check out the instrumentation system. The remaining 25 shots consisted of 19 instrumented with strain gages, and 6 configured for x-ray photography.   Twelve strain gage instrumented shots consisted of the three plate thicknesses mentioned being fired at each of the four rod end configurations.   The purpose of the remaining six shots was to confirm data repeatability, and to provide additional information for later use in evaluating projectile perforation efficiency.

They involved firing .318 cm thickness plates at two hemispherical two 30° cone, one 90° cone, and one flat end configuration rods.

The final shot of the program targeted a .318 centimeter thick plate against a 30° conical nosed rod instrumented with strain gages on both its conical and cylindrical sections, as shown in Fig. 26 of Chapter VI. This shot was fired to determine the amount of strain pulse distortion caused by passage of the strain pulse across cone/cylinder discontinuity of the rods. Since gages on all other applicable shots were bonded to the cylindrical portions of the rods, this information was needed to determine whether a significant error was associated with such gage locations. A description of strain gage locations and gage bonding techniques is presented in Chapter IV.

IV. Experimental Apparatus, Materials, and Procedures

The AFML Low Velocity Gun Range

The experiments upon which this report is based were performed using a low velocity gun range located at the Air Force Materials Laboratory and operated by the University of Dayton Research Institute.

The gun, a general layout of which is shown in Fig. 5 consisted of an unusually short 40 millimeter bore diameter launch tube 91.5 centimeters long with interchangeable chambers and a screw type breech. It was aligned to fire into a 30.5 centimeter cubic target tank where the target rod was mounted. The tank was evacuated before each firing. Behind the target tank was a blast tank and catcher designed to capture all debris generated by a shot and thus prevent damage to the surrounding laboratory. Both sides of the evacuated tank were removable, and contained windows for observing the impact process. Fig. 6 shows the target tank and its interior details.

The target rod was mounted inside a support tube extending from the target tank into the blast tank. The rod was supported with its axis coinciding with that of the gun by six removable tubes passing radially through holes in the main support tube, as depicted in Fig. 6. To ensure a good vacuum seal, the open end of the support tube extending into the blast tank was covered by a thin plastic plate on top of an "O" ring seal. Outside air pressure kept the plate secured when the target tank was evacuated.
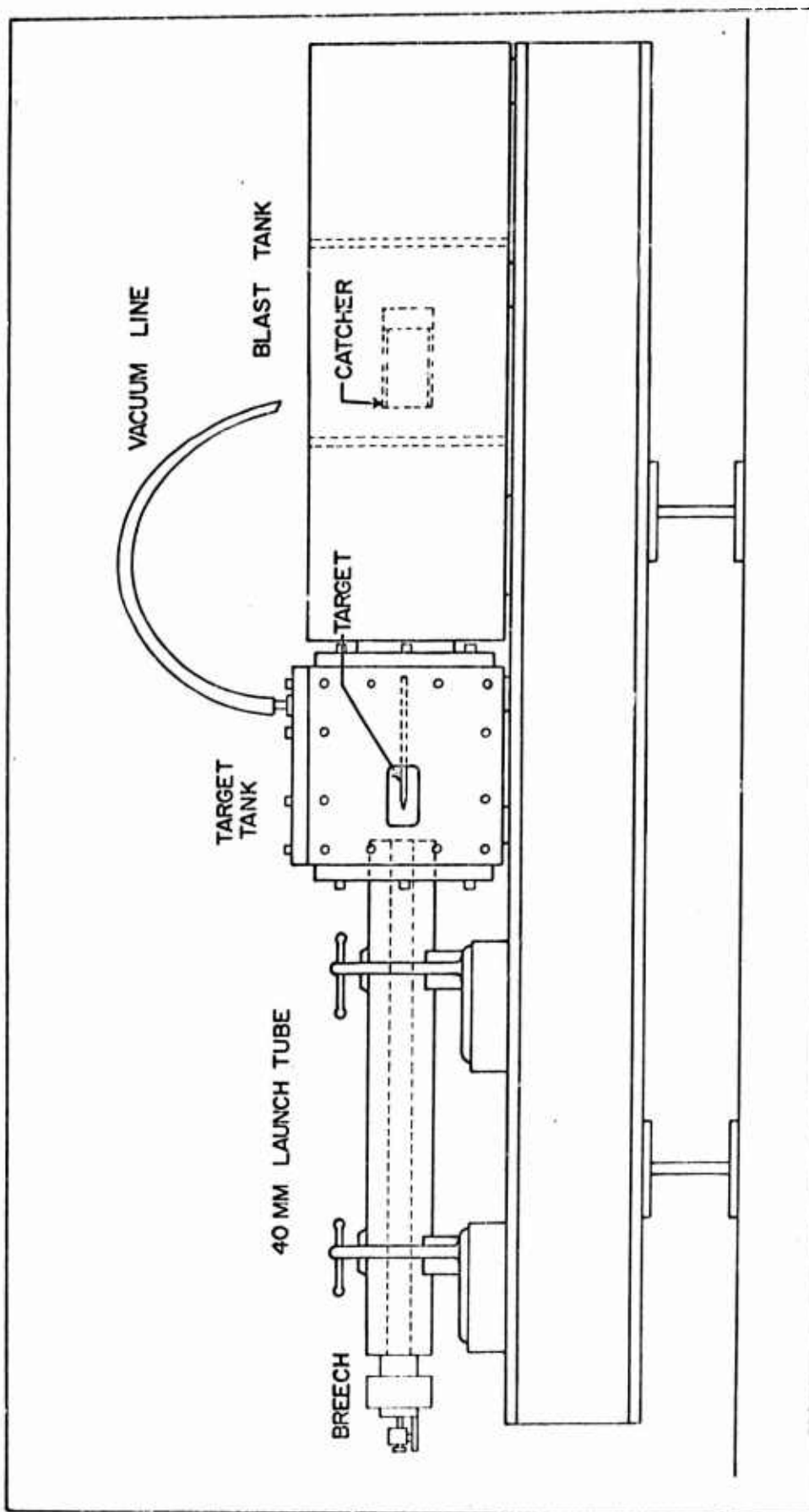
Fig. 5. The Low Velocity Gun Range Assembled to Measure Impact Forces

A switch, used to trigger instrumentation was mounted on the target tank floor just under the forward end of the target rod. Its metal contacts extended up into the gun trajectory so that passage of a sabot closed the switch. Fig. 6 shows a sabot and plate just prior to contact with the switch.

The sabot was propelled from the breech end of the gun by 4 grams of nitro cellulose propellant, initiated by a solenoid activated firing pin which struck a standard shotgun primer. As shown in Fig. 7, the firing pulse came from a 300 volt capacitive discharge system.

Instrumentation

The instrumentation system for this experimental program is depicted in Fig. 7, along with the gun firing circuits. Two Micro Measurements Type EA-06-062AP-120 strain gages bonded to the target rod and an external resistor and potentiometer formed a Wheatstone bridge circuit as depicted in Fig. 7. The output of this bridge was viewed by two channels of a Tektronix Model 551 dual beam oscilloscope, equipped with two Type 1A7A plug-in amplifiers. Two strain gages were used at each location, one on each side of the rod, to double the signal output and cancel out rod bending moments.

The rod used to investigate strain signal distortion was fitted with two additional gages. Another Wheatstone bridge was provided for these, and one of the two oscilloscope channels was connected and used to view the output from the second bridge. Thus the oscilloscope displayed two independent signals simultaneously. Both Wheatstone
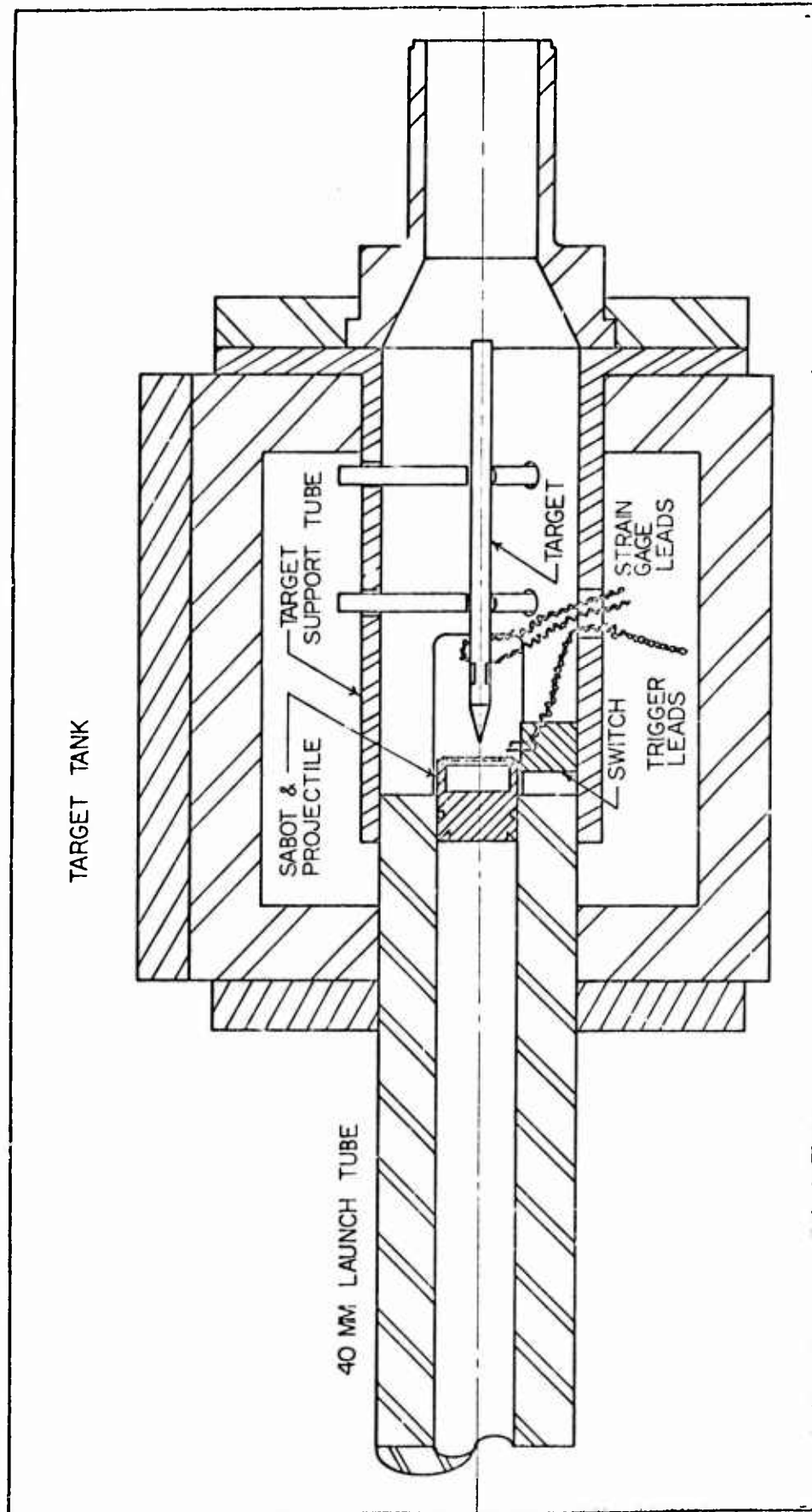
Fig. 6. Details of the Target Tank
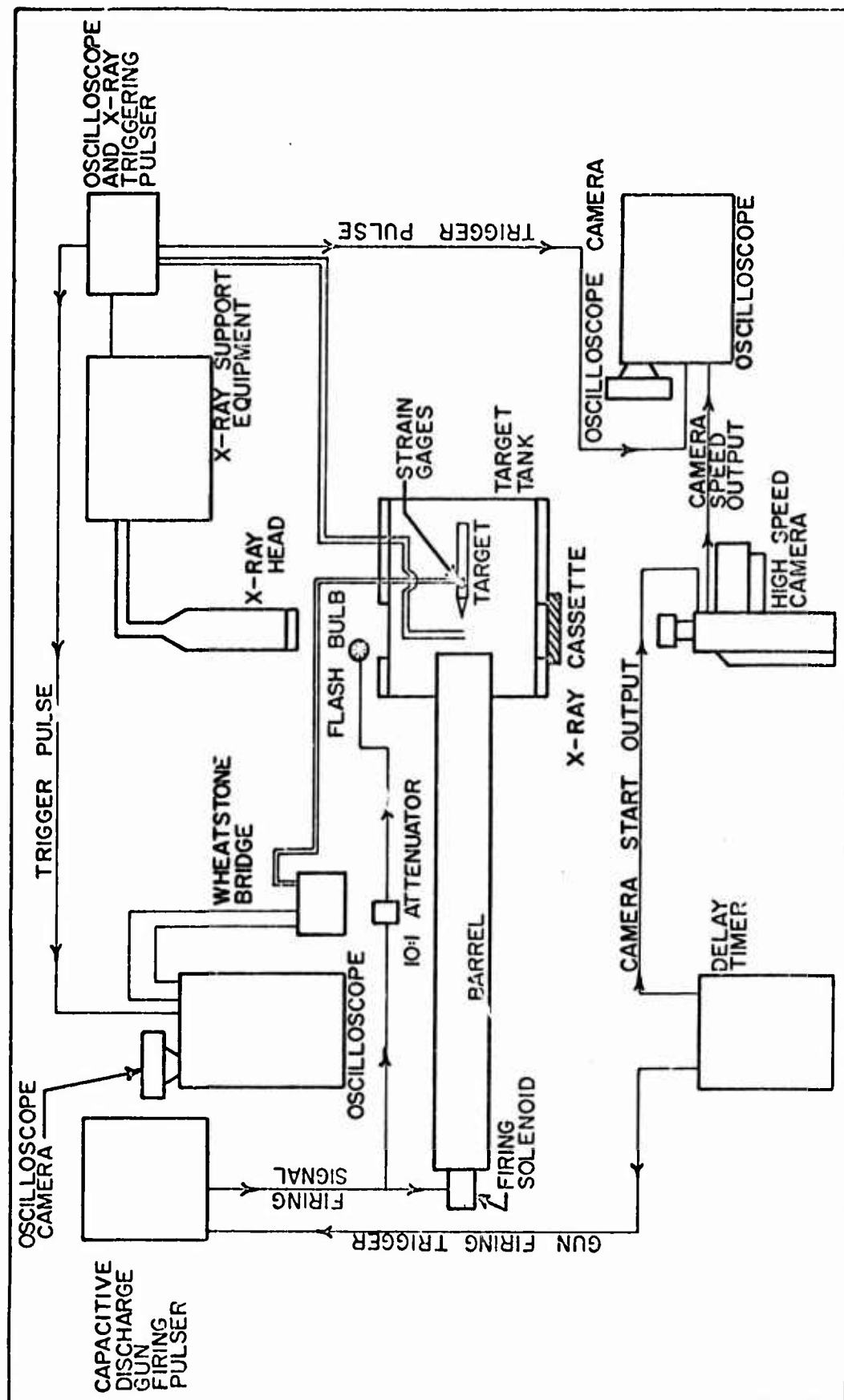
Fig. 7.   The Instrumentation System

bridges were powered by a 6 volt lead acid automobile storage battery whose output voltage was monitored by a precision voltmeter.

The oscilloscope was equipped with a camera which used polaroid Type 47 film to record the rapid beam deflections resulting from a strain signal input. The oscilloscope was triggered by a 45 volt capacitive discharge pulser, which was actuated by the switch set to detect the sabot just before impact occurred.

Sabot velocity was measured with a reel-type streak camera operating in the parallel-slit mode that was set to photograph the leading edge of the sabot as it emerged from the launch tube. Contrary to normal practice, the camera axis was offset by 3° from perpendicular to the sabot trajectory to ensure that only one edge of the sabot was being viewed. A flash bulb connected electrically to the gun firing circuit through a 10 to 1 attenuator, and positioned in front of the target tank window opposite the streak camera, provided illumination for the photography. Its burning time of 1 millisecond was more than adequate to cover the entire perforation process.

In order to establish an accurate relationship between distances on the camera film and distances over which the sabot traveled inside the tank, a special procedure was followed. A clear plastic strip with calibrated distance markings on it was attached to the inner rim of the launch tube, and aligned with its central axis so that the calibration marks were visible through slits in the tank side windows. The camera, in its 3° offset position, was then used to photograph the calibration

marks in exactly the manner used to photograph actual shots. The distance between the longitudinal streaks on the camera film caused by the distance markers on the plastic strip was used to establish the sabot travel--film distance relationship.

The streak camera (Fastax Model WF3) was fitted with a variable reluctance probe that produces electrical impulses whose rate can be related directly to instantaneous camera film speed. These impulses were recorded with a second Tektronix 551 oscilloscope and camera during each shot. As shown in Appendix B, these films were used along with the streak camera film to determine the sabot velocity.

The streak camera starting circuits were set to fire the gun and flash bulb 1.1 seconds after the camera was started. The delay was required to ensure that the camera reached full operating speed before the shot was initiated.

To obtain visual evidence of the perforation process, the instrumentation system included a Field Emission Corporation Model 221 flash x-ray system which produced a burst of 150 kv x-rays with a duration of 20 nsec*. The x-ray head was mounted so that it would flash an x-ray beam through one of the target tank windows, across the front of the target and onto a film cassette mounted outside the target tank on the other side of the trajectory. The x-ray system was triggered by the same switch and capacitive discharge system used for the oscilloscopes.

---

*This flash x-ray system is part of a larger one loaned to AFML by the NASA Manned Spacecraft Center, Houston, Texas.

The x-ray film used was Kodak Type RB-54, and was developed for five minutes in "Dektol" developer.

Sabot Design

A general configuration drawing of the sabots used in this program appears in Fig. 8. The sabots were machined from hard polycarbonate plastic material known by its trade name of "Lexan". Then an aluminum plate of the proper thickness was cemented into a recess at the front end of each sabot with a standard epoxy binder. The sabots were flared slightly at the rear to provide a vacuum seal after they were inserted into the launch tube and to prevent them being drawn along the tube as the target tank was evacuated. To ensure an even better vacuum seal, a rubber "O" ring seal was used near the center of the sabot.

A photograph of the sabot appears in Fig. 9, along with the three thicknesses of plates used in the experiments. On the far left is a
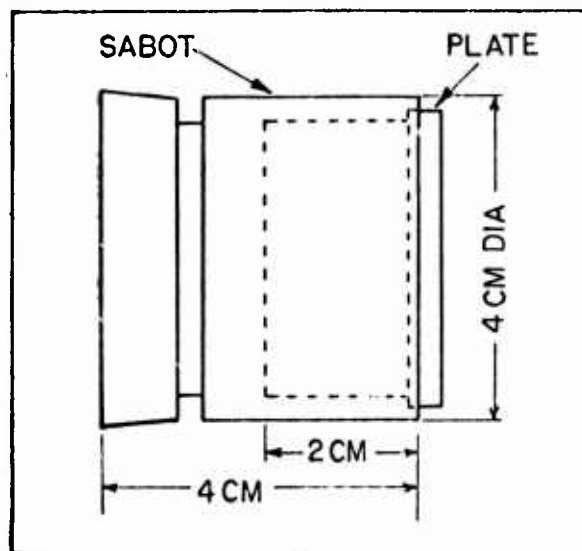
Fig. 8. General Configuration
of the Sabot
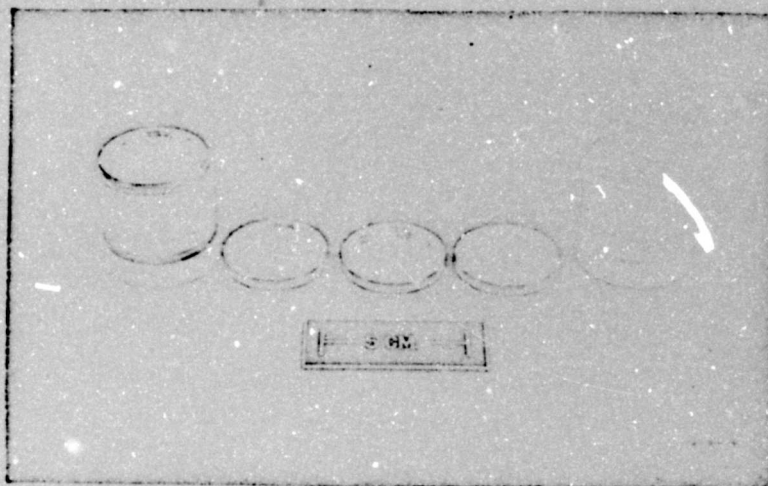
Fig. 9. Sabots and Plates

completed sabot with plate and "O" ring seal in place. On the far right is the basic sabot shell.

Target Design

The four configurations of target rods used in this program are depicted in Fig. 12. Each was machined from steel drill rod and hardened later to Rockwell C-50 to eliminate any permanent yielding during perforation. It is estimated that the yield strength of the rods was in excess of 150,000 Newtons/cm^2.

Two strain gages were then bonded diametrically opposite each other on each rod, 3 centimeters from the tip. This arrangement is depicted in Fig. 11.

Before each gage was mounted, the rod was cleaned with acid. Then a small amount of Eastman 910 or epoxy cement was applied to both
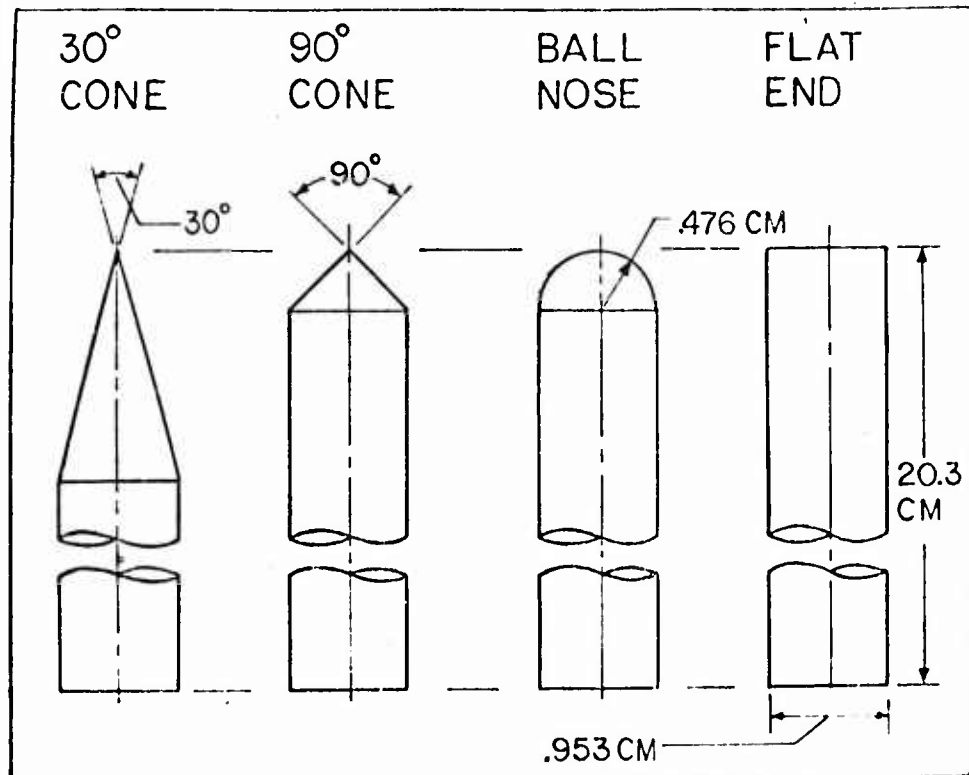
Fig. 10. The Target Rod Configurations
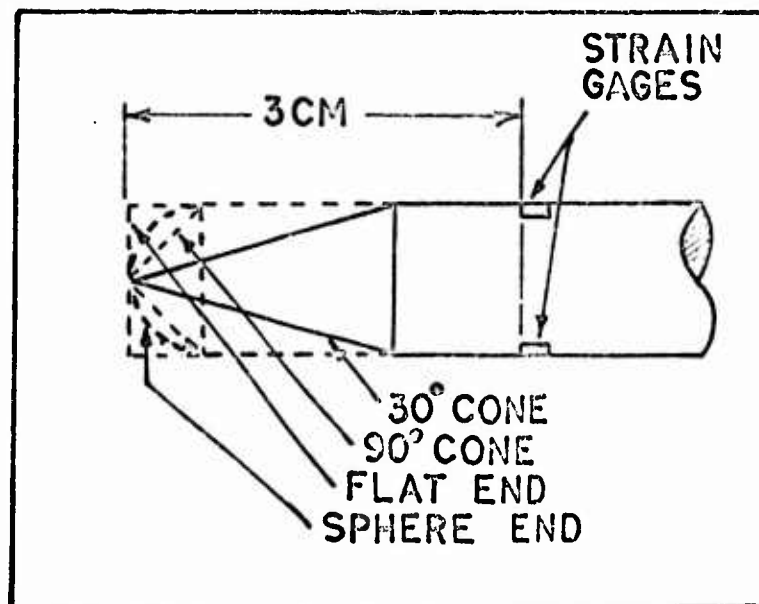
Fig. 11. Strain Gage Location
in Target Rods
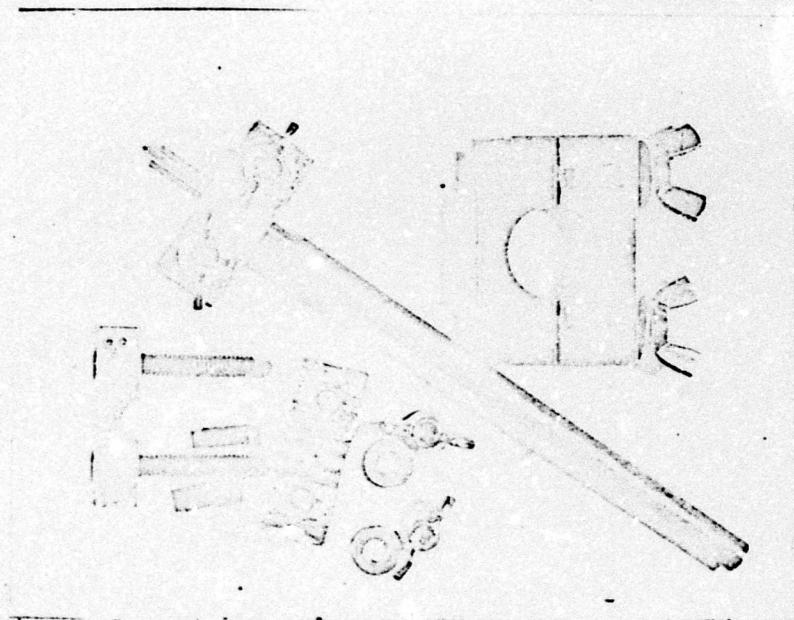
Fig. 12. Strain Gages Clamped to 90° Cone
and Clamp Arrangement

gages and the rod. Both gages were then clamped into position on the rod,

and allowed to cure for 24 hours. Fig. 12 shows gages clamped to a 90°

cone configuration rod, and details of the clamp arrangement.

Experimental Procedures

The experimental procedure for each shot consisted of inserting a

long alignment tool into the breech end of the gun barrel, and pushing it

forward until its far end passed into the target support tube. This portion

of the alignment tool was of the same length and diameter as the target

rod, and was aligned with the gun barrel center line. Six support rods,

made from rolled up plastic sheets, were pushed into holes around the

periphery of the support tube until they contacted the alignment tool and locked into place. The alignment tool was then withdrawn, and the instrumented target rod inserted in its place inside the support tube. Care was taken not to damage the strain gages during this operation. The triggering switch was then installed in the tank as shown in Fig. 6, and wires were connected from the instrument triggering pulser.

As shown in Fig. 6, the procedure just described resulted in the rod resting inside the target support tube and aligned with the central axis of the gun barrel which ensured perpendicular impact between plate and target.

Wires leading from the strain gages were soldered to ones leading from the Wheatstone bridge and passing through a vacuum tight coupling into the target tank. The bridge was then balanced by adjusting a potentiometer in one of its arms, and comparing the position of the oscilloscope beams with the position they had before power was applied to the bridge. Since both amplifiers of the oscilloscope were DC coupled, any voltage across the two signal points of the bridge caused the scope beams to deflect up or down giving it the characteristics of a DC voltmeter. The voltage output of the battery used to power the bridge was monitored continuously throughout the procedure and during the rest of the shot. With periodic recharges, its voltage did not vary perceptibly from 6.19 volts throughout the entire test program.

With the instrumentation assembly complete, a sabot with the appropriate thickness plate bonded to it was inserted into the breech end

of the gun barrel. The test tank was sealed by bolting a plate to the open end of the target support tube. The vacuum pump was then started and allowed to run continuously until completion of the shot.

Film was then loaded into the streak camera and the oscilloscopes set for single sweeps. Then a 12-gauge shotgun casing with the propell-ant load was inserted into the chamber, and the whole assembly screwed onto the breech end of the gun barrel. Shutters on the oscilloscope cameras were then opened, electrical connections were made to the firing solenoid via a Jones Plug and the gun was fired.

The procedure for the x-ray shots was similar to that for the strain gage shots, except that no instrumentation other than the x-ray equipment was used. In particular, the target rods were not equipped with strain gages for these shots.

V. Data Analysis: Assumptions;
Techniques; and Errors

This experimental program relied entirely upon the measurement of strain pulses some distance from the point of perforation to determine the perforation resisting force history. Hence the primary assumption upon which the results of this report are based is that the strain pulses generated by perforation accurately represent the perforation force after application of one-dimensional stress-strain theory and the principles of strain wave propagation discussed in Chapter II. It was further assumed that strain distribution at the strain gage locations was uniform over the plane cross sectional area of the rod.

These assumptions are not arbitrary since each target rod was hardened sufficiently to ensure that its elastic limit was not exceeded during perforation, and research by Goldsmith (Ref 8) indicates that strain pulse distortion becomes significant only after the pulse has traveled distances exceeding those encountered in this program. In addition, one experiment in this program discussed earlier showed no significant strain pulse distortion after the pulse had traversed a sharp discontinuity in slope on the rod.

As described in Chapter IV, data was collected by means of a Wheatstone bridge and oscilloscope connected to the strain gages on the target rod. Changes in gage resistance caused by passage of the strain pulse in the rod were translated into oscilloscope beam deflections that were photographed.

The basic formula for converting oscilloscope strain trace photographs into resisting forces versus time curves is derived in Appendix A as

$$F = \frac{AE \, \Delta e}{2RG \, I_g}$$

(21)

Where F is the perforation resisting force in units of Newtons at some fixed time during perforation, A is the cross sectional area of the rod at the gage location measured in cm^2, Δe is the output voltage of the Wheatstone bridge in volts. R is the electrical resistance of the gage (ohms), G is the gage factor (unitless), and I_g is the electric current passed through the gage. The quantity Δe is obtained from oscilloscope photographs processed with a film reader and the oscilloscope sensitivity settings as described below and demonstrated in Appendix B.

The oscilloscope strain trace was recorded on high speed film and then transferred to a 35 millimeter negative which was read by a digital film reader (Ref 21) to yield values of the strain pulse deflection from a zero reference line at discrete intervals along the time axis of the pulse profile. From a knowledge of the oscilloscope sweep speed measured in microseconds per centimeter, the distances from trace initiation to points on the strain signal were converted directly into a microsecond time base for the pulse. If it is assumed that the point of first strain signal appearance corresponds to the point in time where the plate initially impacts the target rod, then the time base as determined above is also the perforation time base.

Velocities for each experimental shot were computed from records of the streak camera system described in Chapter IV. The camera film was also processed by the digital film reader and velocities were calculated from a knowledge of distances along the film and camera speed. A sample calculation using this technique is presented in Appendix B.

Instrumentation System Error Analysis

From Equation 21 and Appendix A, the strain recorded by the gages is given by

$$\epsilon = \frac{\Delta e}{2RG\, I_g} \tag{22}$$

Where ϵ represents the longitudinal strain in the gage and the remaining quantities were as defined previously. Equation 22 is idealized in that it does not account for inaccuracies in oscilloscope amplifier gain, gage resistance and gage factor and the voltage applied to the bridge. Hence the strain value obtained from Equation 22 and the corresponding force value from Equation 21 will have a tolerance associated with them due to errors in the instrumentation system.

If it is assumed that both A, the specimen cross section and E, the steel modulus of elasticity are quantities that can be measured precisely, then, the error analysis reduces to analyzing Equation 21. The quantity Δe appears in the numerator of Equation 21, hence its increase or decrease will lead to a corresponding increase or decrease in ϵ. It is obtained from the vertical deflection of the oscilloscope beam with respect to a zero baseline and from the oscilloscope amplifier

vertical sensitivity settings. The Tektronix Type 1A7A oscilloscope amplifiers used in this experiment have a vertical sensitivity error of $\pm 2\%$ from indicated deflection, as stated by the manufacturer, but subsequent measurements lead to an estimate that it is closer to 4%. Hence if it is assumed that Δe is the true experimental reading, and δe is its possible variation, then the range of Δe is given by

$$(\Delta e - \delta e) \leq \Delta e \leq (\Delta e + \delta e)$$

(23)

Where

$$\frac{\delta e}{\Delta e} = .04$$

(24)

The quantity R is the strain gage electrical resistance, and has a manufacturers stated tolerance of $\pm .15\%$. If δR is the variation in R, then the range of R is given by

$$(R - \delta R) \leq R \leq (R + \delta R)$$

(25)

Where

$$\frac{\delta R}{R} = .0015$$

(26)

Now G is the gage factor of the strain gages used in this program. It has a tolerance of $\pm .5\%$, as given by the manufacturer. If δG is the possible variation in G, then as before

$$(G - \delta G) \leq G \leq (G + \delta G)$$

(27)

Where

$$\frac{\delta G}{G} = .005$$

(28)

Since the tolerances in R and G are small compared to the tolerance in Δe, they may be neglected.

The quantity I_g is the gage current, which is determined by the Wheatstone bridge power supply voltage, the values of gage and bridge resistances, and the electrical imbalance between the two arms of the bridge. The bridge imbalance was kept to less than one millivolt, which causes a negligible change in gage current. The bridge balance resistances were measured accurately to three decimal places, however the voltmeter used to monitor the bridge power supply voltage had an estimated tolerance of $\pm 1\%$ because the readings were low on the voltmeter scale. Now the gage resistance can vary by $\pm .15\%$, which when compared to the battery voltage tolerance is negligible. From the above, it can be concluded that power supply voltage reading variations dominate the tolerance in I_g. Now since current is proportional to voltage, and if the variation in I_g is designated by δI_g, then the range of I_g is

$$(I_g - \delta I_g) \leq I_g \leq (I_g + \delta I_g)$$

(29)

Where

$$\frac{\delta I_g}{I_g} \cong .01$$

(30)

Now since the quantities R, G, and I_g appear in the denominator of Equation 21, any variation in them will have an opposite effect on ϵ.

Assuming that the worst instrumentation error occurs when all the quantities in the denominator of Equation 21 are at their minimum and Δe is at its maximum, then from the calculations in Appendix C,

ϵ will have a maximum positive error of 5.1% due to instrumentation tolerances.

Errors in the Perforation Time Base Due to Strain Signal Travel Time Differences

A source of error exists in the perforation time base shown on the curves in the next chapter. It arises primarily because of the differing transit times of the strain signal from the point of perforation as the plate moves forward on the "projectile" nose. For data analysis purposes it was assumed that the entire strain signal recorded by the gages eminated from the forward end of the target rod. However, during perforation, the plate moves closer to the gages, resulting in a shorter transit time for the strain signal.

The plate slows down during perforation, hence a more precise time base calculation would have required the integration of a complex plate velocity function at discrete time intervals to get plate distances from the rod tip at these intervals. However it is subsequently shown that the error incurred by not doing so is relatively small. Both Fields and Gabbert have shown that velocity loss during perforation of thin aluminum plates is less than 5% of the initial impact velocity.

Now the greatest time base error occurs during perforation by the 30° cone ended rod because here the plate has the longest distance to travel before perforation is complete. In all other shots, the plate travel distance is smaller by at least a factor of two. The general 30° cone perforation model is depicted in Fig. 13. The strain wave travel time from the tip of

the cone to the strain gages, 3 centimeters away, is 5.86 microseconds,

and from the base of the cone to the gage it is 2.39 microseconds. If it

is assumed that perforation is complete when the plate reaches the base

of the cone, then there will

be an error of 5.86 - 2.39 =

3.47 microseconds in the

perforation time base at this

point. However the error

will be smaller for plate

positions ahead of this loca-

tion. For example, prelim-

inary calculations for one

of the shots assuming con-

stant perforation velocity

showed that peak perfora-

tion force occurred when the

plate was 2.22 centimeters
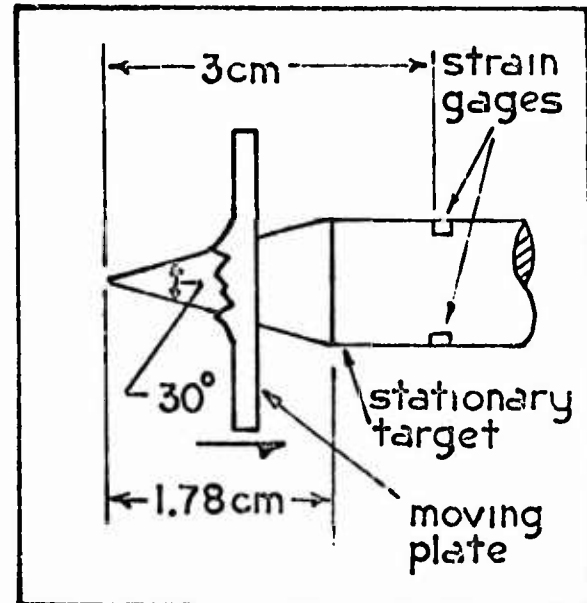
Fig. 13. The 30° Cone
Perforation Model
(Not to scale)

from the strain gages. The difference in strain pulse transit time between

the cone tip and the gages was 1.51 microseconds. This figure is conser-

vative since slowing down of the plate was neglected.

Errors Due to Finite Strain Gage Rise Time

If the combined 10/90 *rise time of the strain gages and instrumen-

tation system is of the same order or longer than the rise time of the strain

---

* Time to rise from 10% to 90% of final value.

pulse, then distortion of the true strain record is to be expected (Ref 1).

Bickle (Ref 1), examines previous work in this area and concludes that

strain gage rise time can be approximated by the expression

$$t_{rg} \leq .8 \frac{L}{C} + .1 \,\mu sec \tag{31}$$

Where t_{rg} is the 10/90 rise time of the gage, L is the gage length and

C is the strain pulse velocity. The gages used in this experimental

program were .119 cm long, and C was calculated to be 5.11×10^5 cm/sec.

Hence

$$t_{rg} \leq .332 \,\mu s \tag{32}$$

The instrumentation system rise time is much shorter than 0.3 μ sec and,

hence, can be neglected relative to this figure.

The shots most affected by strain gage rise time were those invol-

ving flat ended targets. The results of these shots presented in the next

chapter show initial rise times of less than one microsecond, and hence

the possibility exists that these are merely distorted representations of

the true strain record. However, even if the initial pulse slope was

infinite, examination of the shot photographs shows that the net effect

of such a slope increase on the maximum measured amplitude of the strain

record would be negligible.

Errors Due to Strain Pulse Distortion

The worst situation for strain pulse distortion occurs with the

30° cone targets. Here the pulse must travel up a conical section and

then negotiate a discontinuous transition to a cylindrical section before reaching the gages. (See Fig. 13)

The series of experiments conducted by Goldsmith (Ref 8) discussed in the introduction included a 30° cone. Curves for this experiment show the peak strain history in the 30° cone as a function of the distance from the pulse initiation point at the cone apex. Calculations using Goldsmith's curves show an excellent correlation between his experimental strain values and linear strain theory for short distances from the strain initiation point. The maximum distance a strain pulse had to travel along a 30° conical section in any of the perforation experiments was 1.78 centimeters, and no difference between the Goldsmith experimental results and linear theory calculations could be detected for this distance.

As mentioned in Chapter III, a special experimental shot was conducted to determine the amount of distortion generated in a strain pulse when it traverses a sharp discontinuity in rod cross section. A photograph of the oscilloscope traces from this shot and an accompanying figure showing gage locations for each trace are presented in Figs. 26 and 27 (Chapter V). It is apparent from Fig. 26 that pulse distortion under the experimental conditions is negligible, at least for the initial rise portion of the signal. The differences in amplitude of the two signals are due to the difference in cross sectional areas at each gage location. This is demonstrated by the fact that the forward and rear gage location cross sectional areas are .502 and .711 cm^2 respectively and that the corresponding beam deflections at 5 microseconds after impact are 1.8 cm and

1.27 cm. The rear to forward area ratio is 1.416 and the forward to rear deflection ratio is 1.419. These ratios are consistent with the assumption that strain is inversely proportional to the areas over which it acts if there is no energy loss or distortion of the strain pulse as it travels from one location to the next.

Hence from the evidence available, distortions due to strain pulse propagation over a finite distance in the target rods can be neglected safely. If any do exist, they are certainly less than the 5.1% error calculated for the instrumentation system.

Errors Due to Strain Wave Reflection From the Edges of the Plate During Perforation

During the perforation process, strain waves traveled radially outward from the perforation hole in the aluminum plate and reflected to return and distort the strain signal. These distortions appear to follow the peak strain value in some of the oscilloscope photographs presented in the next chapter, and can be characterized as a series of oscillations. Neither cone shaped target showed serious distortion due to this phenomenon, but the hemisphere and flat ended targets did. Calculations show that it takes a stress pulse approximately 6.15 microseconds to travel the distance from the center of the aluminum plate to its outer edge and return, and this is approximately the time after impact when oscillations in the strain record begin to appear.

During the film reading process, an estimate was made of the location of the average value of the signal at the center of the oscillations.

This imaginary line was then assumed to represent the true strain pulse shape, and all force calculations were carried out using beam deflection values thus obtained. It is for this reason that all of the perforation force values for the sphere and flat end targets are only approximations, after 6 to 7 microseconds and should be treated as such.

Errors Due to Nonlinearity in the Oscilloscope Horizontal Sweep

The Tektronix 551 Oscilloscope used in this experimental program had a potential error in its horizontal time base of 3% shortly after calibration. However, an accurate time mark generator check of this time base showed a negligible deviation from the setting on the oscilloscope panel. Hence errors due to nonlinearity in the oscilloscope sweep can be neglected.

VI. Data Presentation, Comparisons, and Discussion

The Perforation Force Versus Time Curves

On the following pages are shown the perforation force versus time curves for the four target end configurations and three plate thicknesses used in this experimental program. As outlined in Chapter III, three plates of differing thickness were fired at each rod end configuration and a number of data confirmation shots followed. For easy comparison, each series of three shots against a single rod end configuration is plotted on the same graph. The plate thickness and velocity are indicated for each shot, and below each graph appears a representative photograph of the oscilloscope traces for that series of shots. Two traces appear on each photograph because both input amplifiers of the dual beam oscilloscope were set to different sensitivities and connected to the same strain gage signal source for most of the shots. The exact peak strain levels for each shot were unknown a priori, hence this technique provided some assurance that all of the signal would not be lost. In each case, the trace used to obtain the perforation force versus time curve is marked with the amplifier input sensitivity in millivolts per centimeter and with the oscilloscope sweep time base. The raw data for plotting all the curves on the following pages appears in Appendix D.

The series of 12 shots comprising of three plate thicknesses and four rod-end configurations are presented first. It should be noted that for some of the shots, the perforation force record ends early due to
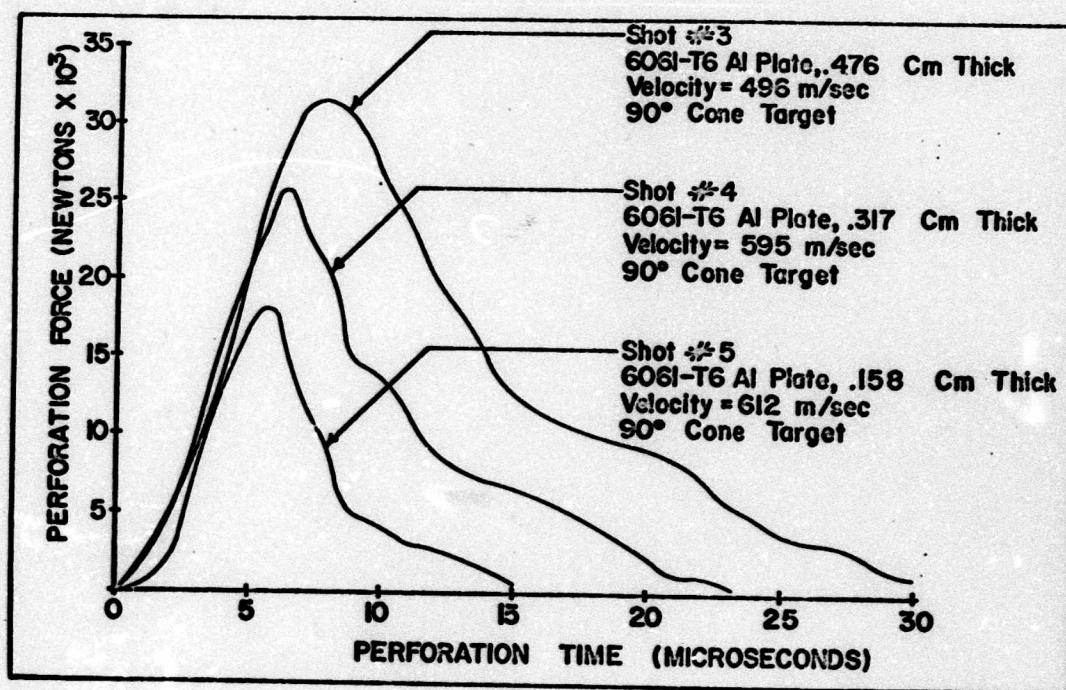
Fig. 14. The 90° Cone Shot Series
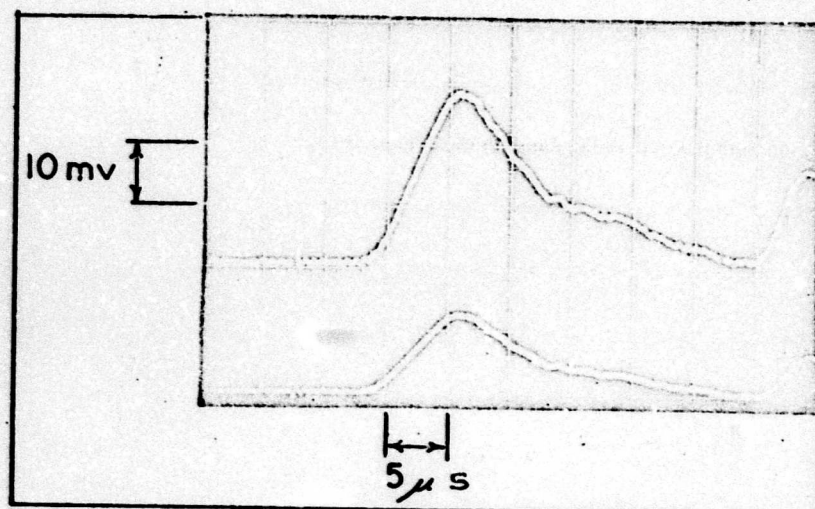
Fig. 15. Shot #3 Oscilloscope Traces
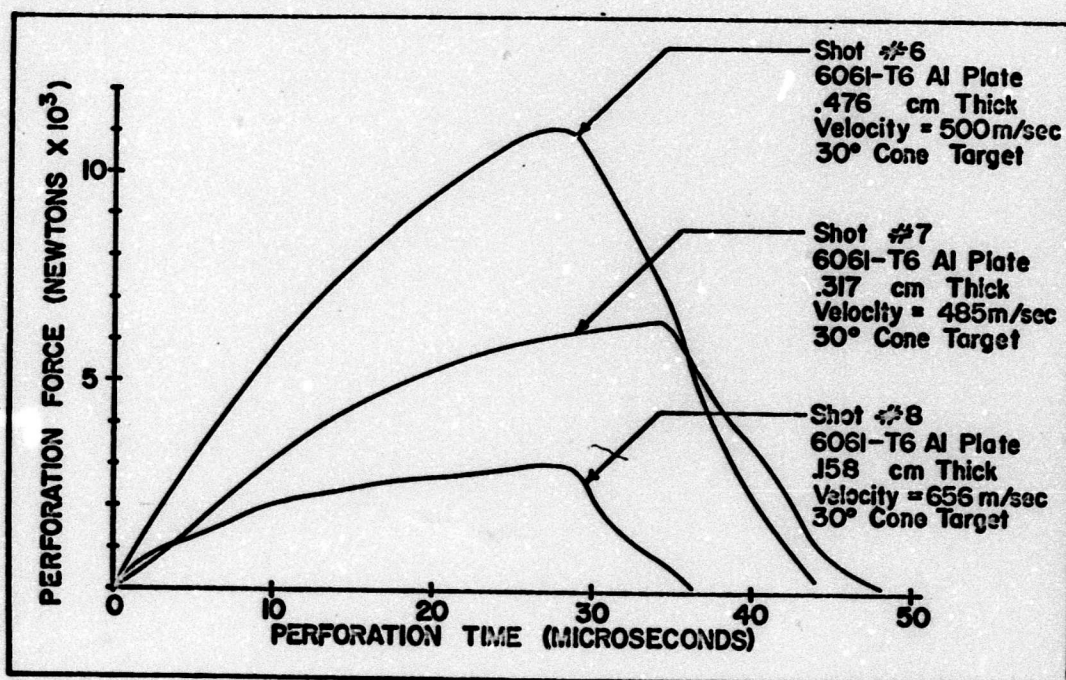
Fig. 16. The 30° Cone Shot Series
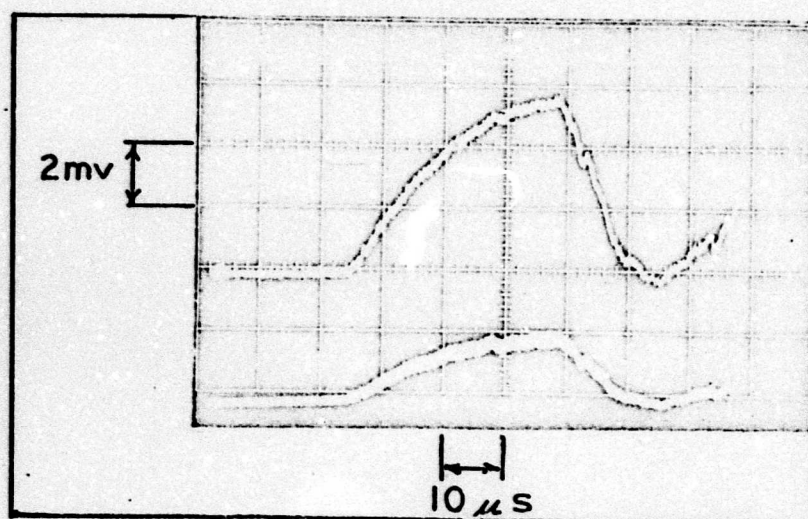
Fig. 17. Shot #7 Oscilloscope Traces

45
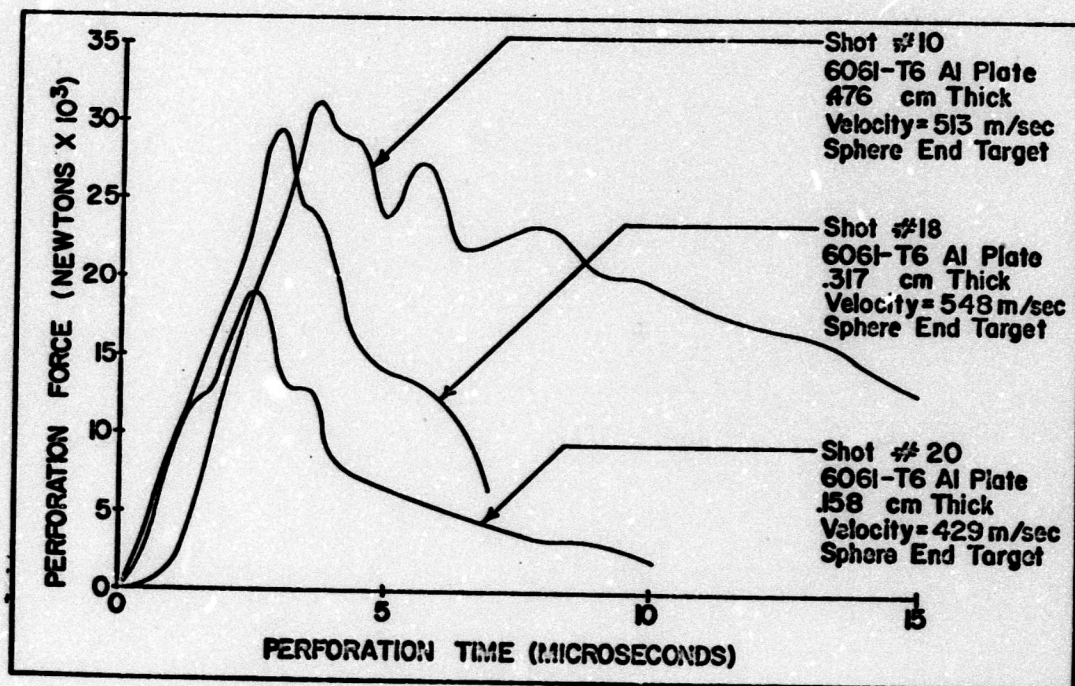
Fig. 18. The Hemispherical Shot Series
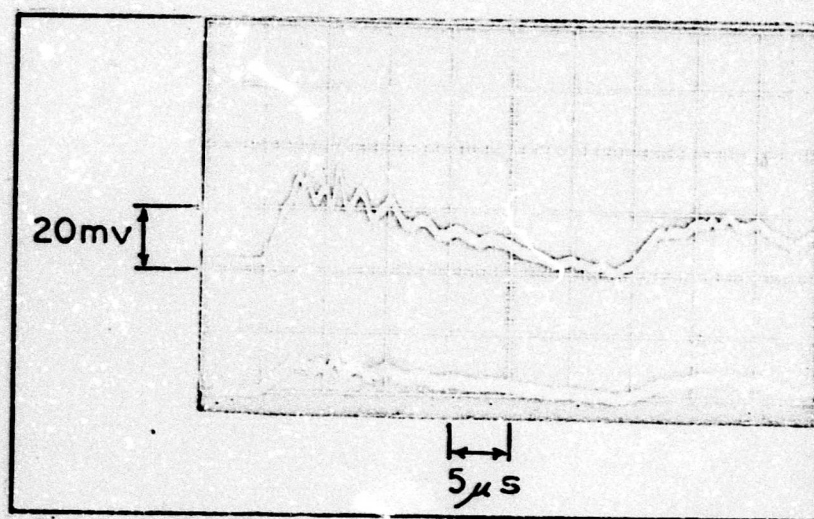
Fig. 19. Shot #10 Oscilloscope Traces

46
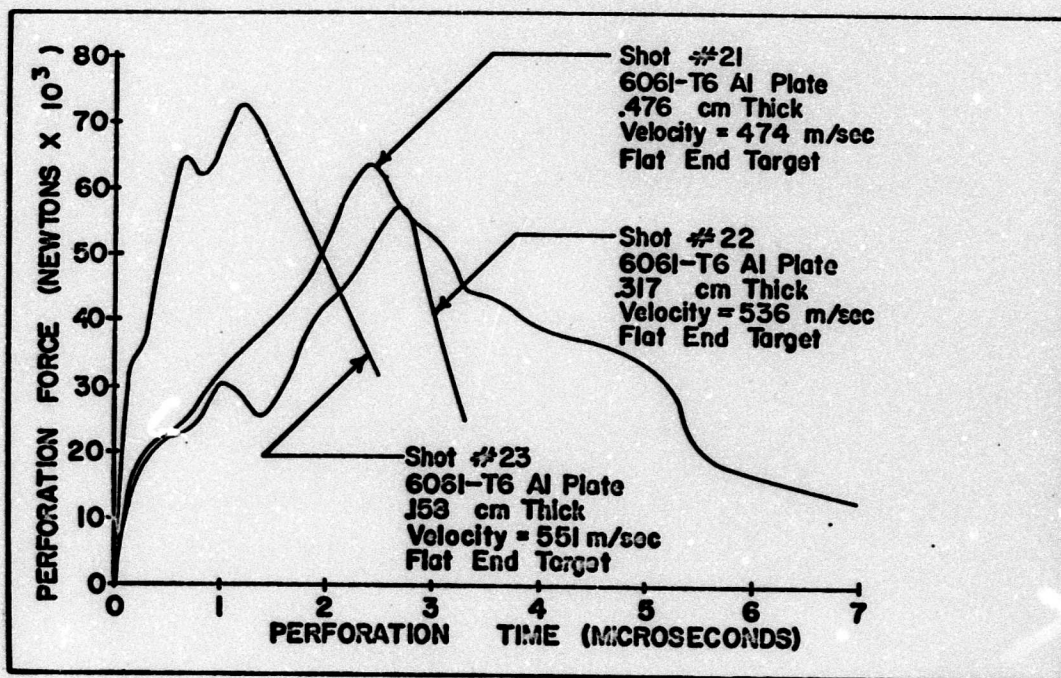
Fig. 20. The Flat-End Target Shot Series
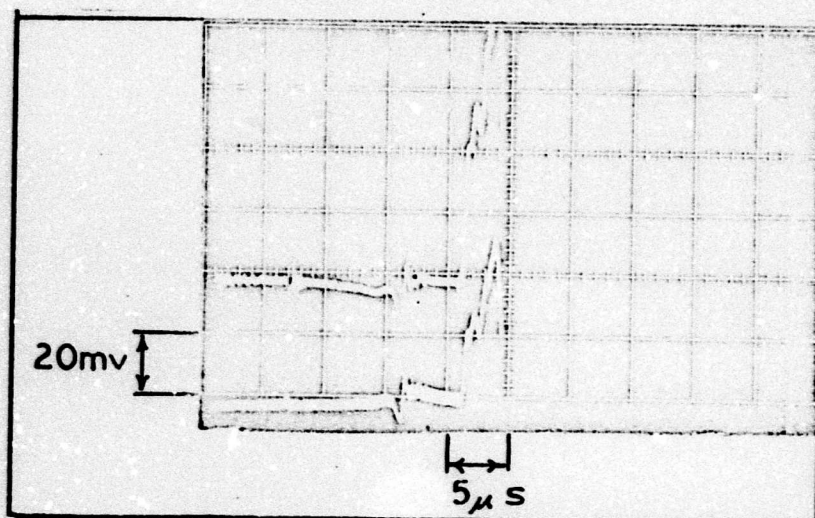
Fig. 21. Shot #22 Oscilloscope Traces
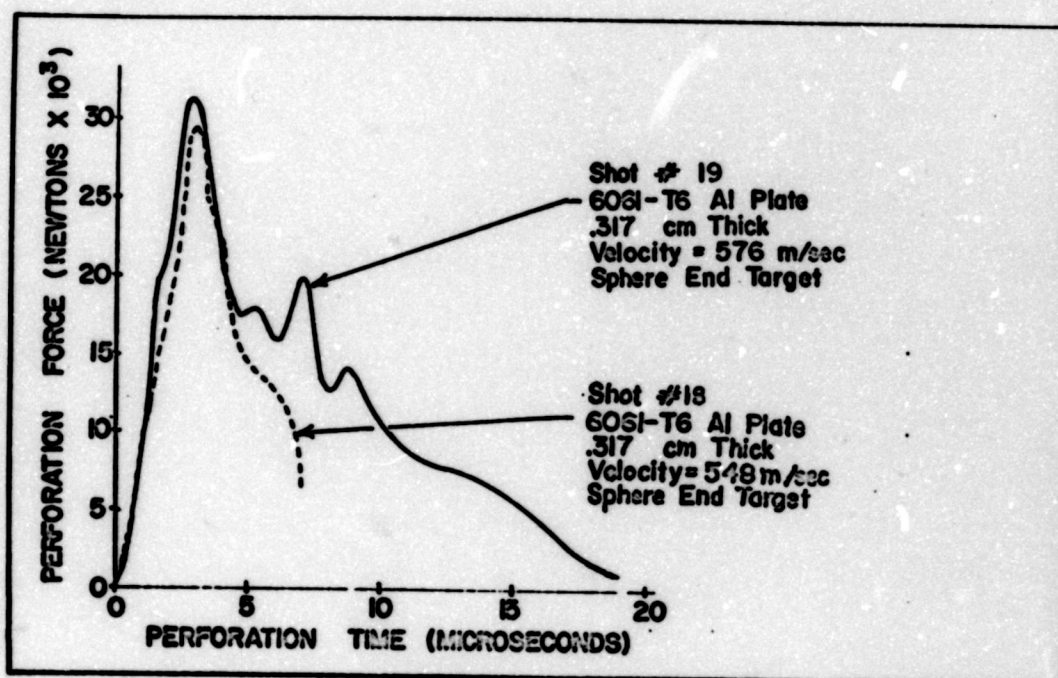
Fig. 22. Data Repeatability Shot #19
With Shot #18 Superimposed
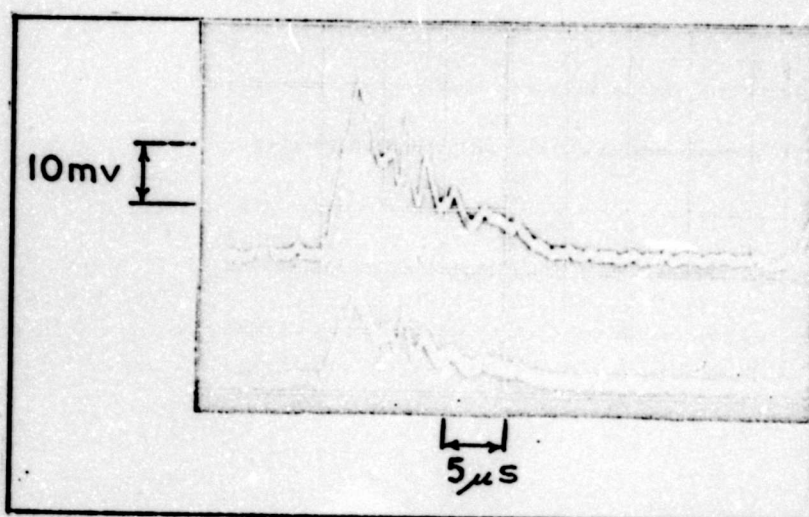
Fig. 23. Shot #19 Oscilloscope Traces
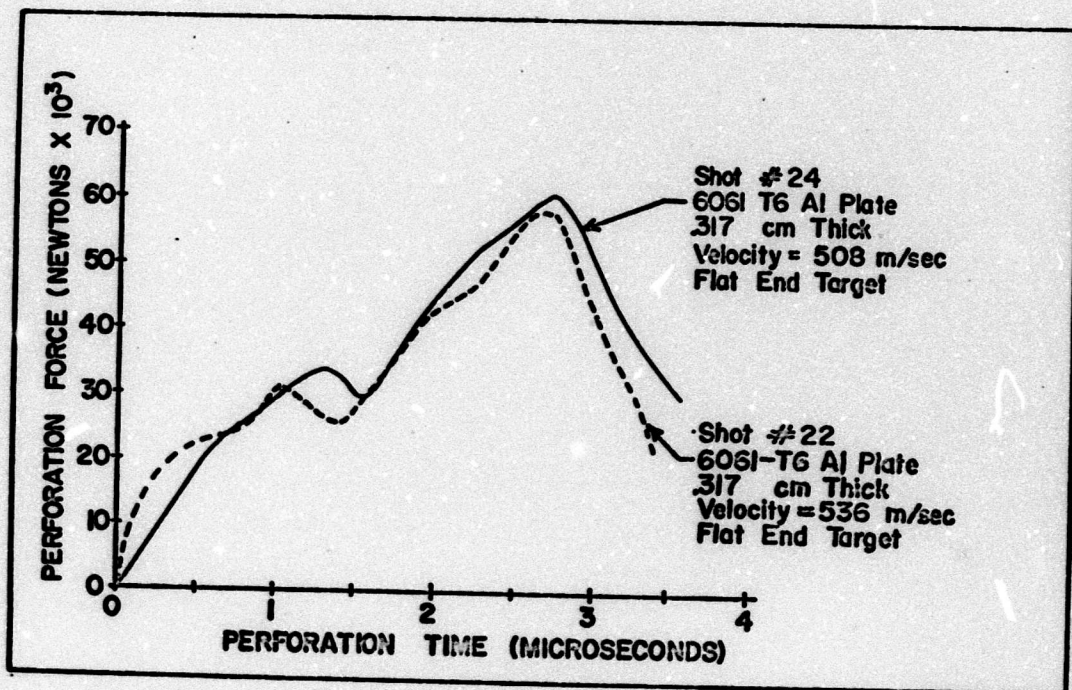
Fig. 24. Data Repeatability Shot #24
With Shot #22 Superimposed
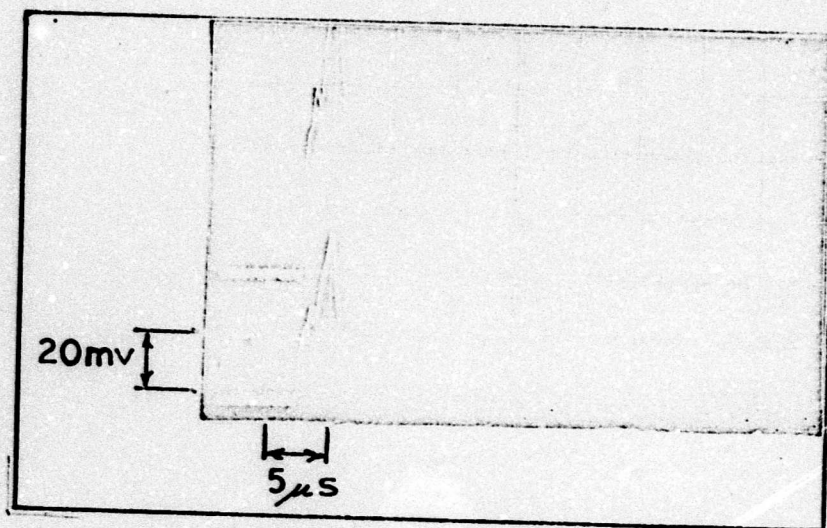
Fig. 25. Shot #24 Oscilloscope Traces

premature strain gage failure.

The results of two data confirmation shots are presented next. In these a .316 cm thick plate was fired at hemisphere and flat ended targets.

Discussion of the Perforation Force Curves

In general, the 12 perforation curves shown reveal considerable differences in both shape and amplitude between the various rod-end configurations. However the curves for each configuration remain similar as the plate thickness is varied.

The highest perforation peak values are exhibited by the bluntest target configurations. For example, the ratio of peak forces between the flat end and 30° cone targets for the same plate thickness is approximately 9 to 1. However the difference between peak forces for the hemispherical and 90° cone targets is only about 1.6 to 1.

All of the shot data presented, except for the flat end series show a trend toward higher peak perforation forces as the plate thickness is increased. In the flat ended target series, the thinnest plate generated the highest peak perforation force. It appears that the total perforation impulse for this case is smaller than for the other two flat shots, though exact comparisons cannot be made due to early gage failure.

The occurance of peak pressures along the perforation time base shows a trend to the left (earlier time) with decreasing plate thickness. This is to be expected since perforation times are also shorter for the

thinner plates. However a comparison of the same configuration Shots #18 and #19 reveals that the peak force for each occurs at 3 and 2.8 microseconds after impact respectively. In connection with this, it is to be noted that the respective velocities on Shots #18 and #19 are 548 and 576 meters per second. Thus it appears that a lower impact velocity can also increase the time to achieve peak perforation force.

The Strain Pulse Distortion Experiment Results

Figs. 26 and 27 show the results of the strain pulse distortion experiment and the corresponding gage locations on the 30° cone target rod. The lower oscilloscope beam shows the front portion of the strain signal just before it transitions to the cylindrical portion of the rod. The upper beam shows the front portion of the pulse after it has transitioned.

The signal from the rear gages exhibits a slower rise time than that from the front gages, but as demonstrated in Chapter IV, this is due to the area difference at the two gage locations. The front portion of the pulse after it has transitioned shows slightly more "ripple" than the incoming pulse, however the difference does not appear to be significant.

X-Ray Photographs of the Perforation Process

All x-radiography shots targeted a .159 cm thick plate against the four target rod configurations. In addition, two shots fired .159 cm plates with no target rod in the tank. These shots were fired to determine the amount of "dishing" the plates experience from launching forces just prior to impact. All shots were fired at an approximate velocity of 755 meters
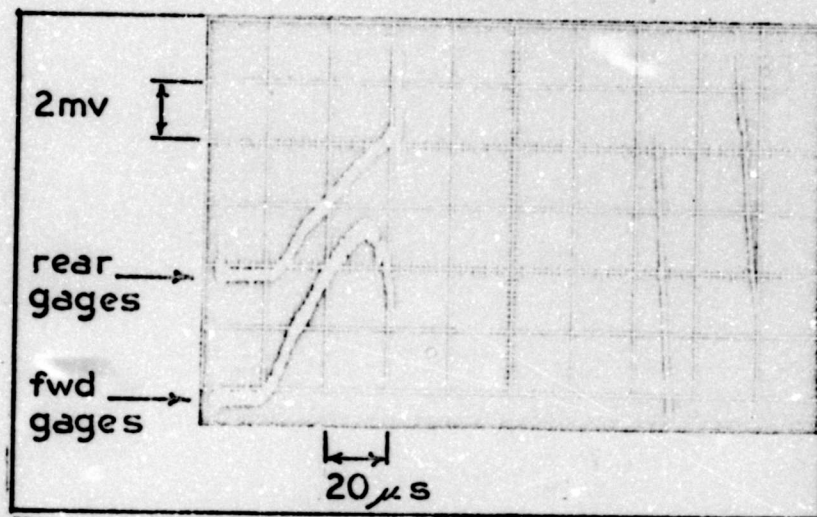
Fig. 26. Shot #30, Strain Pulse Distortion
Experiment Oscilloscope Traces
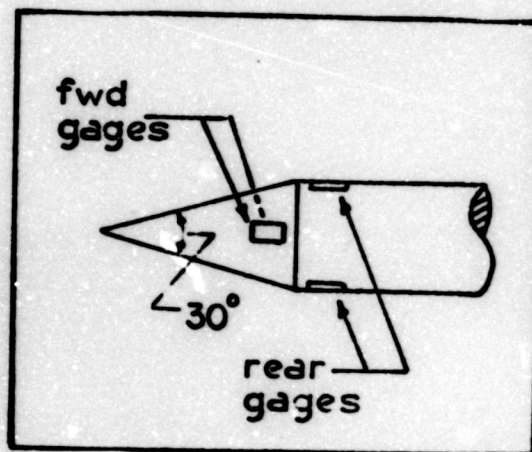
Fig. 27. Strain Gage Locations
for Shot #30

per second (somewhat faster than other experimental shots) to accentuate any dishing tendencies. Figs. 28 through 31 show the four rod configurations perforating the .159 cm thick aluminum plate, and Fig. 32 shows the plate with no target.

Discussion of the X-ray Photographs

In the x-ray photographs, neither of the two cones shows evidence of plug formation, however a plug is clearly visible in front of the flat-ended rod. It is difficult to determine from the x-ray photograph if the hemisphere ended target is generating a plug, but during the course of the experiments, small hemispherical plugs were discovered in the target tank after hemispherical target shots. From this evidence and the radiographs, it appears that hemispherical projectile perforation failure in thin plates occurs through both plugging and petaling. Similarly, the perforation failure mode for the flat-end target is plugging, and both cones cause petaling failure.

It is also to be noted that dishing of the .159 centimeter thick plate at the high velocity with which it was fired is minimal although it
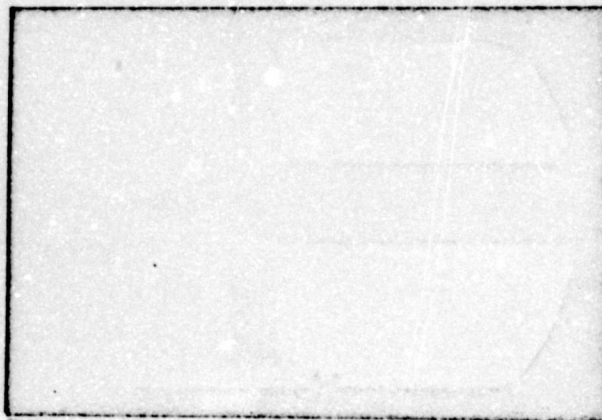
Fig. 28. X-ray Shot #14, 30° Cone
vs. .159 cm Thick Plate
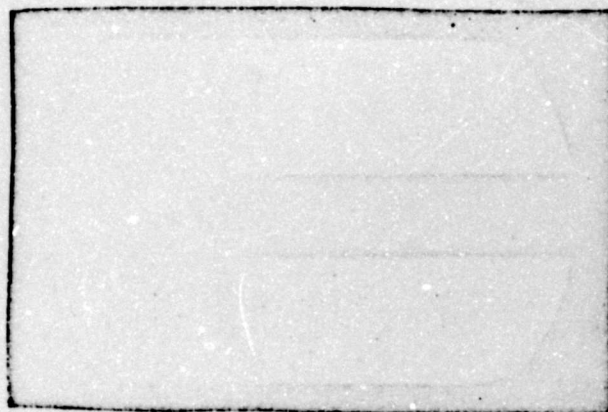
Fig. 29. X-ray Shot #15, 90° Cone
vs. .159 cm Thick Plate

Fig. 30. X-ray Shot #16, Hemisphere
vs. .159 cm Thick Plate

Fig. 31. X-ray Shot #17, Flat End
vs. .159 cm Thick Plate

Fig. 32. X-ray Shot #13, .159 cm Thick
Plate Fired With No Target

can be detected. Hence for the lower velocities of the rest of the experimental   n the dishing phenomenon can be ignored.

Comparisons of P: Data With Previous Results

A. Comparison of Peak Perforation Forces With
Those of Gabbert

As mentioned in Chapter I, Gabbert (Ref 6) conducted a series of quasi-static perforation tests to determine perforation force versus displacement records for hemisphere, flat, and 30° and 90° cone-end configuration perforators. Tests were carried out against .476, .318, and .159 centimeter thick aluminum plates. Since these are the same end configurations, plate thicknesses and plate materials used in this experimental program, a direct comparison of peak force values obtained is possible.

Gabbert did not run a complete test program where all projectile-end configurations were tested against three plate thicknesses. Only the hemispherical configuration was tested in this manner. The 30° and 90° cones were each used to perforate a .318 centimeter thick plate, and the flat-ended rod was tested only against .476 and .318 centimeter thick targets. Table I compares the peak perforation forces from this experimental program with those obtained by Gabbert.

As can be seen in Table I, ordnance velocity peak perforation forces for the spherical and flat ended projectiles are

Table I

Comparison of Peak Perforation Forces

Projectile Configuration	Plate Thickness (cm)	Ordnance Velocity Peak Force (Newtons)	Peak Force From Ref 6 (Newtons)
30° Cone	.476	11,200	N/A
	.318	6,573	8,125
	.159	2,972	N/A
90° Cone	.476	31,648	N/A
	.318	25,832	13,400
	.159	18,192	N/A
Hemispherical	.476	31,226	22,900
	.318	29,391	12,230
	.159	19,050	5,920
Flat End	.476	63,626	27,400
	.318	57,227	17,000
	.159	73,269	N/A

significantly greater than those obtained from Ref 6. However the one comparison available for the 30° cone shows a higher peak force for the quasi-static perforation experiment. The higher ordnance velocity peak forces can be explained by considering that dynamic inertial forces present in the quasi-static tests. However no physical explanation is readily apparent for the 30° cone peak force anomaly.

B. Perforation Efficiency Comparisons

The comparisons of perforation efficiency are made by deriving a theoretical value for the decrease in velocity known

projectiles would experience when subjected to the perforation impulses obtained in this experimental program for the same projectile shapes. Then the projectile with the smallest velocity loss will be the most efficient perforator.

For this comparison the perforation force versus time records for Shots 24, 19, 4 and 7 were plotted on the same graph as shown in Fig. 24. They were also plotted on graph paper with a density of 8 squares per centimeter, and the area under each curve determined by counting squares. The number of squares for each shot was converted to the perforation impulse in Newton-seconds by application of the appropriate horizontal and vertical scale factors to a rectangular area made up of this same number of squares. These impulses were then assumed to be applied to typical projectiles of the same configuration fired by both Fields (Ref 5) and Gabbert (Ref 6) against the same plate thickness. Then the resulting velocity decrease was calculated for each.

Now examination of data from Fields and Gabbert shows that there is, in general, a linear decrease in velocity loss during perforation as impact velocity increases. Thus to make the results more comparable, the values of theoretical velocity loss calculated previously were multiplied by an impact velocity ratio. If the impact velocity for the shot in this program was greater than for the corresponding shot of either Fields or Gabbert, the velocity loss was multi lied by a ratio where the greatest impact
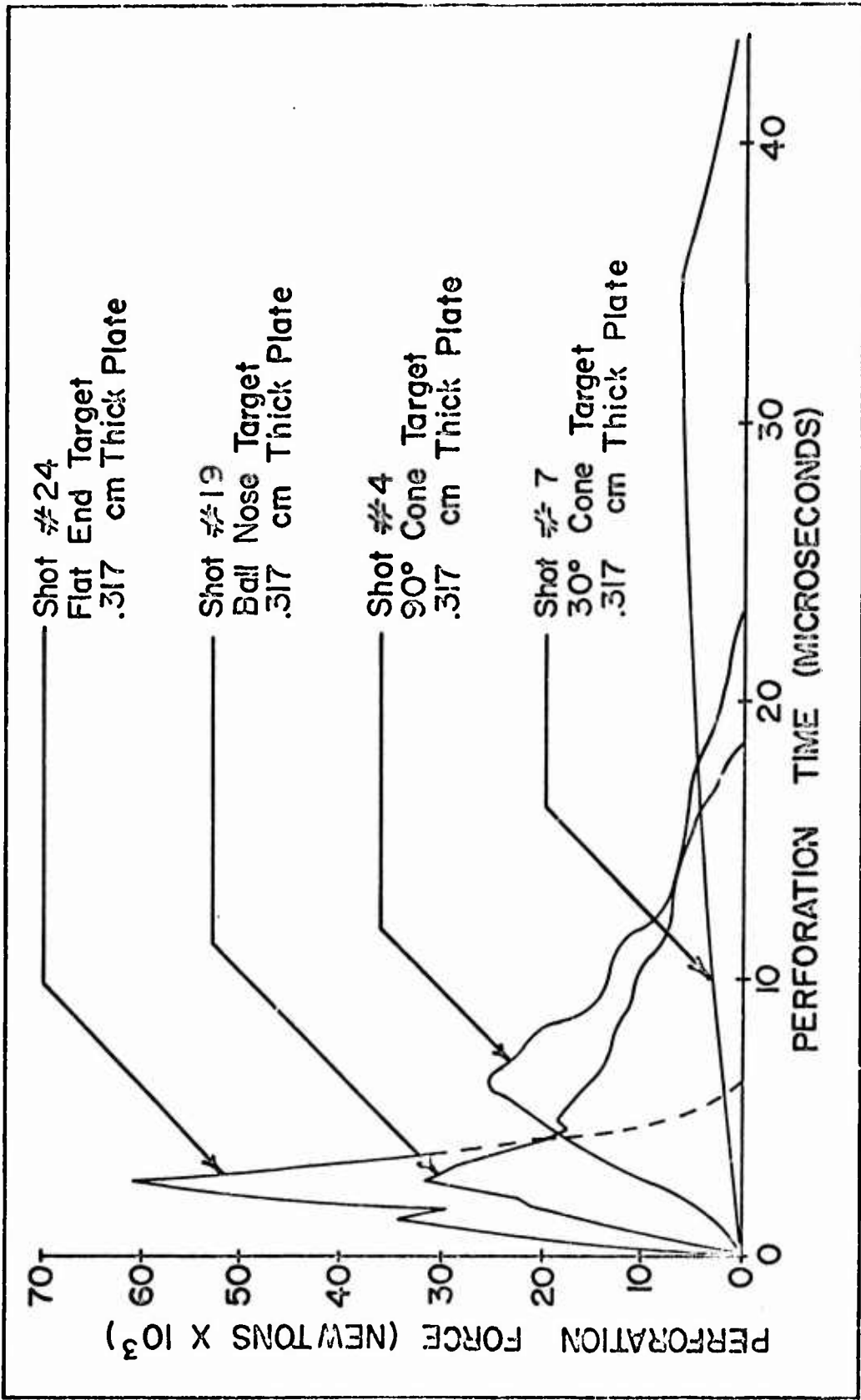
Fig. 33. Perforation Efficiency Comparison Plot of Shots 4, 7, 19, and 24

velocity was placed in the numerator. If the Fields or Gabbert impact velocity was greater, then the reverse procedure was followed.

The results of the previous calculations show that the theoretical velocity losses of the typical Fields and Gabbert projectiles are three to five times lower than those measured experimentally, when these projectiles are subjected to the perforation impulses for the same projectile shape and plate thickness obtained from Fig. 33. However the experimental procedure used to obtain the perforation force curves in Fig. 33 consist d of firing a plate at a stationary rod of about 100 grams mass, where both Fields and Gabbert fired approximately 20 gram projectiles at stationary plates. Both the projectiles and rods were of the same diameter, but their length and mass differed approximately by a factor of five. If it is now assumed that the sabots and plates used in this experimental program are held stationary while the 20 centimeter long 100 gram rods are fired at them with the same impact velocities that Fields and Gabbert fired their projectiles, the impact momentum is approximately five times as great as in their experiments. Hence for purposes of comparison, the theoretical velocity decreases calculated by applying perforation impulses to Fields and Gabbert projectiles are multiplied by a ratio of rod mass to projectile mass to get a new value for the velocity decrease. This approach is used

because the results of Ref 22 show that it is not unreasonable

to assume that velocity decrease during perforation is inversely

proportional to the mass of the projectile, providing all other

initial conditions are equal.

The results of the previous discussion are summarized

in Table II. The second column of this table shows impulses

calculated from Fig. 33, the third gives the masses of the projec-

tiles fired by either Fields or Gabbert to which these impulses are

applied to give the velocity loss values of the fourth column. In

the sixth column, these velocity losses have been corrected for

impact velocity as described earlier. The eighth column gives

the velocity losses corrected for projectile impact mass, and

the ninth gives the corresponding experimental values obtained

by either Fields or Gabbert.

C. Comparison of a Semi-Empirical Value of the Ratio of
    Final to Initial Perforation Velocities With Experimental
    Values Obtained From Reference 6

The theoretical development in Chapter II leads to

Equations 10, 12, and 17 which predict velocity after perforation

as a function of the parameters K, n, and the perforation time t_p.

The data collected in this program was not extensive enough to

predict accurate values for K and n, and thus a comprehensive

evaluation of this theory is not possible. However an approxi-

mate value of K can be obtained from the peak force values of

Table II

Perforation Velocity Loss Calculation Results

Projectile Configuration	Impulse From Fig. 33 (Newtons-sec)	Projectile Mass (gms)	Velocity Loss Uncorrected (m/sec)	Velocity Loss Corrected For Impact Velocity (m/sec)	Rod Mass (gms)	Rod Mass To Projectile Mass Ratio	Velocity Loss For Impact Mass (m/sec)	Velocity Loss Experimental (m/sec)
30° Cone	.122	22.16 (Ref 6)	5.4	4.83	105.9	4.78	23.1	24.94 (Ref 6)
Flat Cylinder	.1076	19.87 (Ref 5)	5.36	5.66	112.9	5.68	32.2	26.61 (Ref 5)
Hemisphere	.154	20.94 (Ref 6)	7.35	7.67	112.5	5.38	43.6	29.30 (Ref 6)
90° Cone	.139	19.82 (Ref 5)	7.00	8.23	111.6	5.63	46.4	30.05 (Ref 5)

Shots 18 and 19 and their corresponding impact velocities by making some simplifying assumptions. Then by assuming that $n = 1$, a value of v_f/v_o obtained from Equation 17 for a given projectile shape and mass can be compared with that obtained experimentally for the same projectile. The experimental data for this comparison is from Gabbert (Ref 6).

Now Equation 17 states that

$$\frac{v_f}{v_o} = \exp\left[-\frac{K}{mv_\star} \, t_p\right] \tag{17}$$

As a matter of convenience, the normalizing factor $v_\star$ will be taken as the speed of a stress pulse in a steel bar some distance from the point of initiation. Then

$$v_\star = 5.11 \times 10^3 \text{ meters/sec} \tag{33}$$

Gabbert conducted two shots in which hemispherical nose projectiles were targeted against .317 cm thick 6061-T6 aluminum plates. These are labeled as Shots 1 and 14 in his thesis results, but to avoid confusion with the experimental data in this report, they will be referred to as Shots 1_G and 14_G in the following analysis. Now shots 1_G and 14_G had the same plate thickness and projectile configuration as Shots 18 and 19 in this program, hence an approximate value of K determined from the latter can be used to calculate v_f/v_o for the former by means of Equation 17.

From Equation 2 of Chapter II,

$$F(t) = K\left(\frac{v}{v_\star}\right)^n \tag{2}$$

63

or for n = 1

$$F(t) = K\left(\frac{v}{v_*}\right)$$

(13)

Thus if values of F(t) are plotted against values of (v/v_*) for Shots 17 and 18, K can be approximated by the slope of the line drawn between the two points. Since Gabbert's data shows that velocity loss during perforation for the hemispherical nosed projectile is less than 5% of the impact velocity, v in Equation 13 will be assumed to equal the impact velocity for Shots 17 and 18 even though $\Gamma(t)$ is taken to be the peak perforation force in each case. For the same reason, perforation time t_p for both of Gabbert's shots will be calculated by dividing the projectile length by the impact velocity.

Now Shots 18 and 19 have impact velocities of 548 and 576 meters per second respectively. Hence for Shot 18, (v/v_*) = .1072 and for Shot 19, (v/v_*) = .1129. Also the peak perforation forces for Shots 18 and 19 respectively are 29,391 and 31,488 Newtons. Then an approximate value of K is given by

$$K \cong \frac{31,488 - 29,391}{.1129 - .1072} \text{ Newtons}$$

(34)

or

$$K \cong 3.68 \times 10^5 \text{ Newtons}$$

(35)

Now for Gabbert's Shot 1_G, the impact velocity was 501 meters per second and the projectile length was .0304 meters. Hence

$$t_p = \frac{.0304}{501} = 6.06 \times 10^{-5} \, \text{sec}$$

(36)

The mass of this projectile was .02068 kilograms, hence from

Equations 17, 35, and 36, the calculated value of (v_f/v_o) is

given by

$$\left(\frac{v_f}{v_o}\right)_c = \exp\left[-\frac{(3.68 \times 10^5)(6.06 \times 10^{-5})}{(2.068 \times 10^{-2})(5.11 \times 10^3)}\right]$$

(37)

or $\quad \left(\dfrac{v_f}{v_o}\right)_c = .81$

(38)

Now the experimental velocity loss for Shot 1_G was 32 meters

per second so that the experimental value of (v_f/v_o) is given by

$$\left(\frac{v_f}{v_o}\right)_E = \frac{501-32}{501}$$

(39)

or $\quad \left(\dfrac{v_f}{v_o}\right)_E = .935$

(40)

Similar calculations using Shot 14_G data give values of $(v_f/v_o)_c$

and $(v_f/v_o)_E$ as .82 and .944 respectively. These results are

summarized in Table III.

It is obvious from this limited number of calculations that

for the specific case where n = 1, the theoretical development in

Chapter II predicts a 13 to 13.4 per cent higher velocity loss for

a hemispherical nosed projectile than determined experimentally.

However due to the extremely limited amount of data available,

Table III

A Comparison of Experimental and Calculated
Residual to Impact Velocity Ratios

Shot	$(v_f/v_o)_E$ From Ref 6	$(v_f/v_o)_C$	% Error*
1_G	.935	.81	13.4
14_G	.944	.82	13.13

*with respect to the experimental value

no conclusions will be made concerning the validity of this

theory.

VII. Conclusions and Recommendations

Conclusions

In general, it can be concluded from the data in Chapter VI that the thicker a target, the higher will be the peak force acting on a projectile during perforation at ordnance velocities. This conclusion assumes that target material properties do not change as the thickness is increased, and does not take into account the apparent anomaly of the flat end configuration shot against a .159 cm thick plate shown in Fig. 20. Here the peak force is highest for the thinnest target plate tested. No other series of shots exhibit this characteristic, so it is possible that very blunt projectiles targeted against plates less than .16 centimeters thick will occasionally encounter higher peak forces but smaller perforation impulses than those fired at thicker plates. However the experimental program was not extensive enough to confirm this hypothesis.

It is further concluded that pointed projectiles encounter much lower peak perforation forces than blunt projectiles under the same conditions. However, as is clearly demonstrated by Fig. 33, this reduction in peak force is accompanied by an increase in perforation time which tends to keep the perforation impulse a constant. This in turn leads to conclusions about relative perforation efficiency of the projectile shapes tested.

Referring to Table II of Chapter VI, it appears that the 30° cone shaped projectile is the most efficient perforator of all. It shows the lowest velocity decrease during perforation after the corrections have

been applied for impact velocity and projectile mass. This is in general agreement with Fields' conclusions since he finds the pointed projectiles which petal the target are more efficient perforators than shapes which plug the target. Fields did not fire any 30° cone projectiles, however his "optimal" projectiles were very close to this configuration.

Similarly it can be concluded that the next most efficient perforators after the 30° cone are the flat ended cylinder, the hemisphere, and the 90° cone in that order. Again, Fields did not fire any hemispherical projectiles, but he found that the flat cylinder is a more efficient perforator than the 90° cone. This too is in agreement with the conclusions just reached.

Even though the flat cylinder appears to be a more efficient perforator than the hemisphere or 90° cone, it has a much higher aerodynamic drag coefficient than either or these. Hence the impact velocity of a flat ended projectile after several hundred meters of travel in air would be considerably lower than that of a cone or hemisphere fired with the same initial conditions.

The final conclusion to be reached from the results of this study is that static perforation tests do not accurately predict the peak forces projectiles experience during perforation of thin plates at ordnance velocities. This conclusion is reached from Table I of Chapter VI, where the peak force differences between static and dynamic tests are as high as 300%.

Recommendations

The results of the flat end shot series in this program show deviations from patterns established by the other shots. It is therefore recommended that another 20 to 30 shots be conducted where flat ended projectiles are impacted by plates less than .5 centimeters thick. This firing sequence would be carried out to see if clear relationships between peak perforation force, impact velocity, perforation impulse, and plate thickness can be established.

It is further recommended that future experiments using the techniques developed in this program be run with a larger range of velocities, more plate thicknesses and a more varied selection of projectile shapes. Oblique impact shots can also be run after a modification of the plate and sabot shapes used in this program. It is also recommended that the target "projectile" suspension system be modified to allow for the support of very short projectiles instrumented with strain gages. This would give a more realistic simulation of the perforation process, since it would partially correct for the differences in impact momentum discussed in Chapter VI.

Finally, it is recommended that in order to reduce the distortion of the strain signal due to reflections from the edges of the plate during perforation, a larger plate be fired at the stationary "projectile". A threefold increase in the plate diameter would increase the strain pulse transit time from the projectile to the plate edge and back to approximately 18 microseconds.

Bibliography

1. Bickle, L. W. "The Response of Strain Gages to Longitudinally Sweeping Strain Pulses." Experimental Mechanics, 7:12, 541-544 (December 1967).

2. Bluhm, J. I. "Stresses in Projectiles During Penetration." Proc. of Soc. for Exp. Stress Analysis, 13:2, 167-181 (1956).

3. Bluhm, J. I. "The Measurement of Dynamic Strains Induced In Projectiles During Penetration of Armor Plate." Technical Report WAL-TR-760/420, Watertown Arsenal Laboratories, (December 1957).

4. Cunningham, D. M. and W. Goldsmith. "Short Time Impulses Produced by Longitudinal Impact." Proc. of Soc. for Exp. Stress Analysis, 16:2, 153-162 (1959).

5. Fields, T. E. "The Effect of Projectile Shape on Ballistic Perforation of Thin Metal Plates." Technical Report AFML-TR-69-202, July 1969, Air Force Materials Laboratory, Wright-Patterson Air Force Base, Ohio.

6. Gabbert, R. D. "An Investigation of Perforation Mechanics in Thin Aluminum Plates." Thesis, June 1970, Air Force Institute of Technology, Wright-Patterson Air Force Base, Ohio.

7. Goldsmith, W. "Analytical Versions of Penetration Processes." NAVWEPS Report 7812, February 1962, U. S. Naval Ordnance Test Station, China Lake, California.

8. Goldsmith, W. and V. H. Kenner. "Elastic Waves in Truncated Cones." Experimental Mechanics, 8:10, 442-449 (October 1968).

9. Goldsmith, W. Impact. London: Edward Arnold (Publishers) Ltd., 1960.

10. Hughes, D. S. and W. L. Pondrum and R. L. Mims. "Transmission of Elastic Pulses in Metal Rods." The Physical Review, 75:10, 1552-1556 (May 1949).

11. Kolsky, H. Stress Waves in Solids. Oxford: The Calendron Press (Publishers)., 1953.

12. Kornhauser, M. Structural Effects of Impact. Baltimore: Spartan Books (Publishers) Inc., 1964.

13. Masket, A. V. "The Measurement of Forces Resisting Armor Penetration." J. of Appl. Physics, 20:132-140 (February 1949).

14. Nishiwaki, Jien. "Resistance to the Penetration of a Bullet Through an Aluminum Plate." J. Phy. Soc. of Japan, 6:334-378 (October 1951).

15. Prescott, J. Mechanics of Particles and Rigid Bodies. London, New York, Toronto: Longmans, Green, and Co. (Publishers)., 1947.

16. Raftupolos, D. and M. Al-Salihi. "Elasto-Plastic Wave Interaction in Impact." Technical Report 3, September 1968, Department of the Army Contract No: DAAD05-67-C-0586.

17. Rinehart, J. S. "On Fractures Caused by Explosions and Impacts." Quarterly of the Colorado School of Mines, 55:4, 1-55 (October 1960).

18. Sears, F. W. Mechanics Heat, and Sound. Addison-Wesley Publishing Company, (Publishers) Inc., 1958.

19. Sedgwick, R. T. "Theoretical Terminal Ballistic Investigation and Studies of Impact at Low and Very High Velocities." Technical Report AFATL-TR-68-61, May 1968, Air Force Armament Laboratory, Eglin Air Force Base, Florida.

20. Suh, P. N. "Stress Wave Propagation in Truncated Cones Against a Rigid Wall." Experimental Mechanics, 7:12, 541-544 (December 1967).

21. Swift, H. F., et. al. "An Inexpensive Automatic Digital Film Reader." Paper prepared by the University of Dayton Research Institute, Dayton, Ohio for presentation at the 16th Meeting of the Aeroballistic Range Association, 1969.

22. "The Resistance of Various Metallic Materials to Perforation by Steel Fragments." Project Thor Technical Report No. 51, (Confidential), April 1963, John Hopkins University, Baltimore, Maryland.

23. Thompson, W. T. "An Approximate Theory of Armor Penetration." J. of Appl. Physics, 26:1, 80-82 (January 1955).

Appendix A

Derivation of the Strain Gage
Data Evaluation Formula

Fig. 34 represents a generalized version of the Wheatstone bridge

circuit used in this experimental program. The following notation applies

both to the circuit and to the derivation of the strain gage reduction

formula:

v – bridge power supply value in volts

I_g – gage current in amperes

e_g – voltage across gage

R – gage resistance in ohms

ΔR – change in gage resistance due to applied strain

r – bridge balance resistance in ohms

Δe – Wheatstone bridge signal output in volts

Δe_g– change in voltage across gage due to applied strain

G – gage factor, dimensionless

Referring to Fig. 25, with the bridge properly balanced, the

resistance in both branches is equal and no potential difference appears

between points 1 and 2. Then Δe = 0 and

$$I_g = \frac{V}{R+r} \qquad (41)$$

$$e_g = I_g R \qquad (42)$$
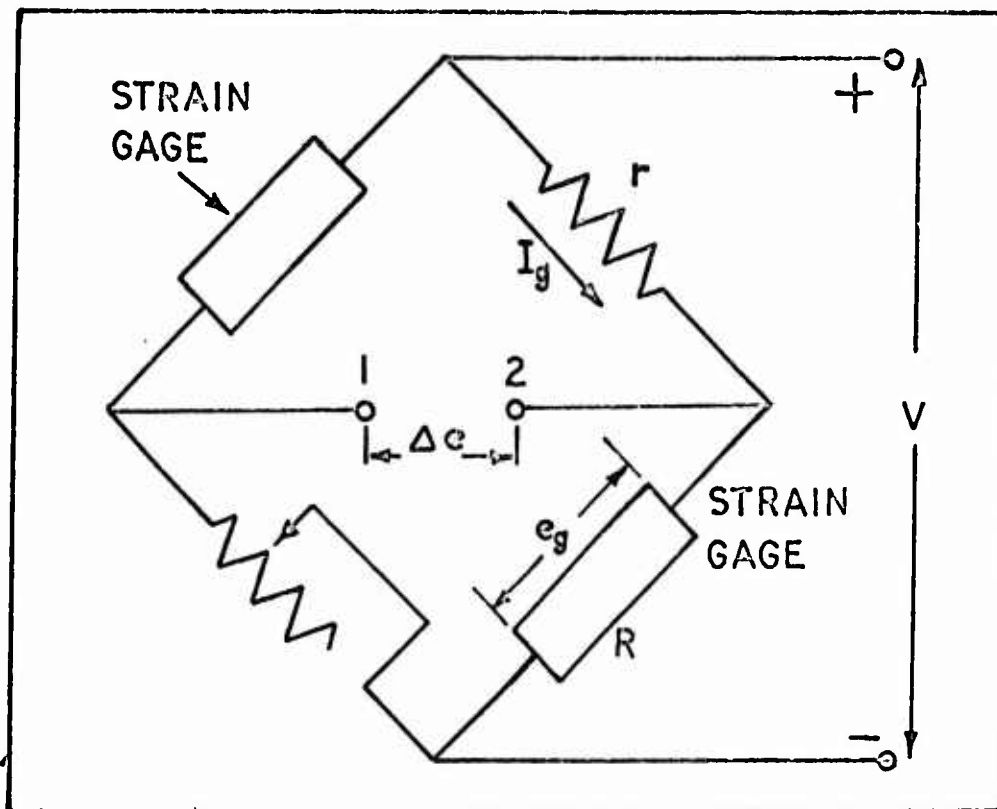
Fig. 34. Wheatstone Bridge Strain Gage Circuit

If a strain pulse of the same sign and value is now applied to both gages, their resistance will change by a value R. Now if $\Delta R \ll$ r + R and the internal impedance of the signal sensing device connected between points 1 and 2 is high compared to all other impedances in the bridge circuit, then the resulting variation in I_g is negligible. Then for each gage

$$\Delta e_g = I_g \Delta R$$

(43)

If ΔR for both gages is positive, then by Kirchoff's Law the voltage at point 1 with respect to the negative terminal of the power supply will decrease by a value Δe_g . Similarly the voltage at point 2 will increase by the same amount. Hence a differential voltmeter or oscilloscope

73

connected between points 1 and 2 will read a value of $2\Delta e_g$. Hence it is concluded that

$$\Delta e = 2\Delta e_g \tag{44}$$

or from Equation 37

$$\Delta e = 2 l_g \Delta R \tag{45}$$

The gage factor is defined by the manufacturer as

$$G = \frac{\Delta R/R}{\epsilon} \tag{46}$$

Where ϵ is the strain applied to the gages. Then from Equations 45 and 46, we get Equation 22 of Chapter V

$$\epsilon = \frac{\Delta e}{2RGl_g} \tag{22}$$

Now for strains below the elastic limit of the material to which the strain gages are bonded and from Equation 20 of Chapter II

$$F = AE\epsilon \tag{20}$$

Where F is the force which causes the strain ϵ , A is the area across which the strain is acting and E is the elastic modulus of the material to which the gages are bonded. Then combining Equations 20 and 22, we get Equation 21 of Chapter IV as

$$F = \frac{AE\Delta e}{2RGl_g} \tag{21}$$

connected between points 1 and 2 will read a value of $2\Delta e_g$. Hence it is concluded that

$$\Delta e = 2\Delta e_g \qquad (44)$$

or from Equation 37

$$\Delta e = 2 l_g \Delta R \qquad (45)$$

The gage factor is defined by the manufacturer as

$$G = \frac{\Delta R/R}{\epsilon} \qquad (46)$$

Where ϵ is the strain applied to the gages. Then from Equations 45 and 46, we get Equation 22 of Chapter V

$$\epsilon = \frac{\Delta}{2RG l_g} \qquad (22)$$

Now for strains below the elastic limit of the material to which the strain gages are bonded and from Equation 20 of Chapter II

$$F = AE\epsilon \qquad (20)$$

Where F is the force which causes the strain ϵ, A is the area across which the strain is acting and E is the elastic modulus of the material to which the gages are bonded. Then combining Equations 20 and 22, we get Equation 21 of Chapter IV as

$$F = \frac{AE\Delta e}{2RG l_g} \qquad (21)$$

Appendix B

Sample Calculations

Oscilloscope Film Reading Conversion to Perforation Force

The oscilloscope strain data films were read by means of a film reader whose output was connected to a digital voltmeter (Ref 21). Hence the difference in voltage between any two vertical points on the film could be correlated directly to the actual distance between these points.

The first step in the film evaluation process was to record a voltage reading for the strain pulse baseline, then voltage readings were taken at two grid marks representing 1 centimeter vertically. Since the sensitivity of the oscilloscope in volts per centimeter was known, this latter operation established a relationship between voltage readings on the voltmeter and the oscilloscope beam deflection voltage .

Then from Chapter IV, the perforation force is given by

$$F = \frac{AE \, \Delta e}{2RG \, I_g}$$

(21)

Where A is in cm^2, E in Newtons per cm^2, R is in ohms, and I_g is in amperes.

This calculation uses Shot #3 as an example. For Shot #3, the baseline voltage reading on the digital voltmeter was 4.564 volts and the two voltage readings 1 centimeter apart vertically were 3.880 and 3.121 volts respectively. Now the oscilloscope vertical sensitivity was .01 volt/cm, hence the ratio of film reader volts to one oscilloscope volt was

given by

$$\frac{3.880 - 3.121}{.01} = 75.9 \tag{47}$$

For Shot #3, the peak perforation force occurs at 7.6 microseconds after impact and the film reader voltage at this point was 2.467. Hence the total deflection of the oscilloscope beam from the baseline at this point in terms of film reader volts was

$$4.564 - 2.467 = 2.097 \tag{48}$$

Hence

$$\Delta e = \frac{2.097}{75.9} = .02763 \text{ volts} \tag{49}$$

Now gage current was calculated to be

$$I_g = .0257 \text{ amp}$$

and: $\quad R = 120 \text{ ohms}$

also: $\quad A = .7125 \text{ cm}^2$

$$E = 20.7 \times 10^6 \frac{\text{Newtons}}{\text{cm}^2}$$

$$G = 2.085$$

then

$$F = \frac{(.7125)(21.1 \times 10^6)(.02763)}{2(120)(2.085)(.0257)} \tag{50}$$

or

$$F = 31,700 \text{ Newtons} \tag{51}$$

Velocity Calculation From Streak Camera Film Data

Fig. 35 depicts that portion of the 16 millimeter streak camera film which contained the velocity data, and Fig. 36 shows the oscilloscope trace from which camera film speed was determined. For this sample calculation, Shot #6 is used as an example.

In Fig. 35, 7.62 millimeters is the distance between any two successive film holes, and the time between any two successive peaks on the oscilloscope trace in Fig. 36 is the time required for the film to move this distance. The distance D in Fig. 35 is the distance the leading edge of the sabot moves in the same time that it takes the film to move a
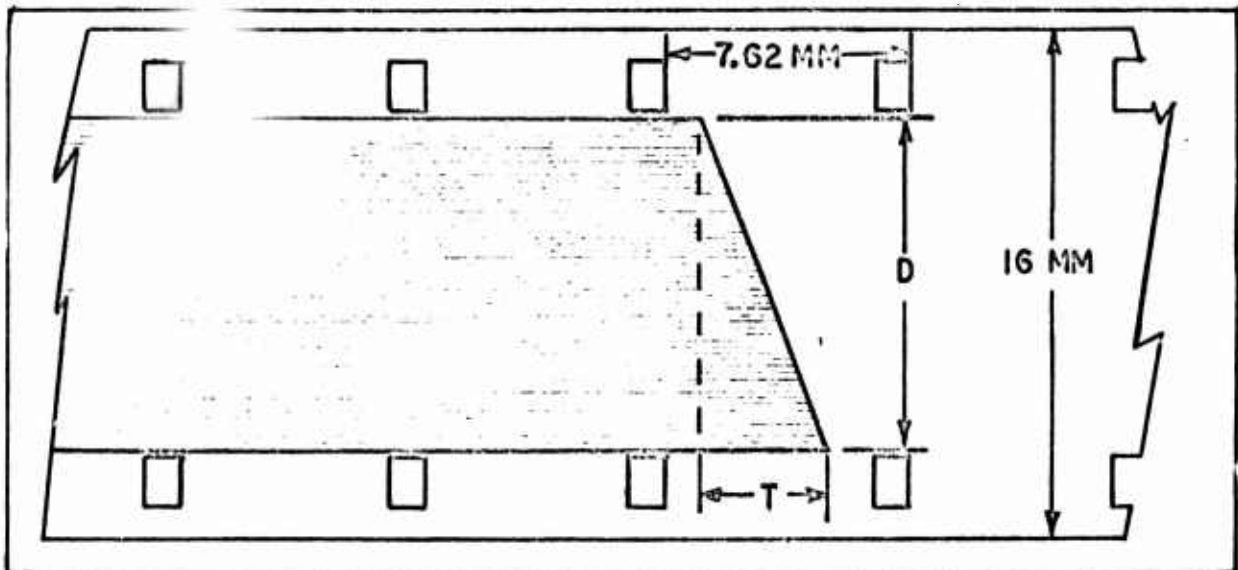
Fig. 35. Streak Camera Velocity Determination Film Trace
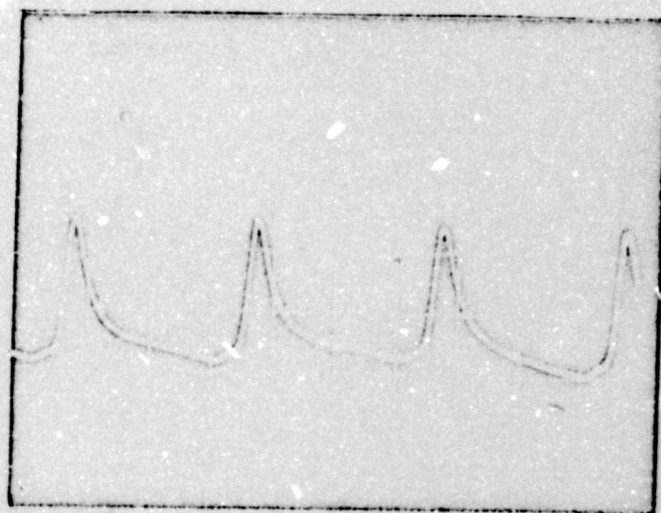
Fig. 36.   Shot #6 Streak Camera Speed
Oscilloscope Trace.   Time
Base = 50 s per division

distance T. D is not a true interval on the film because the sabot and

the camera were separated by approximately 60 centimeters. The interval

T was determined by means of a film reader after each shot.

Now if t is the time it takes the film to move 7.62 millimeters,

then the time it takes the film to move a distance T is given by t_T, where

$$t_T = \frac{T t}{7.62}$$

(52)

But t_T is also the time that it takes the sabot to move the distance D.

For all shots it was determined experimentally, as described in Chapter

IV, that

$$D = 30 \, mm$$

(53)

Then sabot velocity in millimeters per second can be calculated

from

$$V_s = \frac{D}{t_T}$$

$$\text{(54)}$$

or

$$V_s = \frac{7.62\ D}{Tt}$$

$$\text{(55)}$$

Now for Shot #6, t is determined from the oscilloscope film as 148.3 microseconds = 1.483×10^{-4} seconds. Interval T was measured to be 3.08 millimeters. Then from Equation 55

$$V_s = \frac{(7.62)(30)}{(3.08)(0001483)} \quad \frac{mm}{sec}$$

$$= 5 \times 10^5\ \frac{mm}{sec}$$

$$\text{(56)}$$

$$= 500\ \text{meters/sec}$$

$$\text{(57)}$$

Appendix C

Instrumentation System Error Analysis Calculation

From Chapter V we have from Equation 22 that

$$\epsilon = \frac{\Delta e}{2RGI_g}$$

(22)

Where the range of each quantity in this expression is:

a. $(\Delta e - \delta e) \le \Delta e \le (\Delta e + \delta e)$ (23)

$$\frac{\delta e}{\Delta e} = .04$$

(24)

b. $(R - \delta R) \le R \le (R + \delta R)$ (25)

$$\frac{\delta R}{R} = .0015$$

(26)

c. $(G - \delta G) \le G \le (G + \delta G)$ (27)

$$\frac{\delta G}{G} = .005$$

(28)

d. $(I_g - \delta I_g) \le I_g \le (I_g + \delta I_g)$ (29)

$$\frac{\delta I_g}{I_g} = .01$$

(30)

Now for a maximum positive error

$$\epsilon_M = \frac{(\Delta e + \delta e)}{2(R - \delta R)(G - \delta G)(I_g - \delta I_g)}$$

(58)

where ϵ_M designates the maximum positive value of ϵ due to instrumentation tolerances. Then the maximum positive error in the strain reading due to instrumentation tolerances is

or. $$\% \, error(\epsilon) = 100 \left[\frac{\epsilon_M - \epsilon}{\epsilon} \right] = 100 \left[\frac{\epsilon_M}{\epsilon} - 1 \right]$$

(59)

Now

$$\frac{\epsilon_M}{\epsilon} = \frac{RGI_g(\Delta e + \delta e)}{\Delta e(R - \delta R)(G - \delta G)(I_g - \delta I_g)} \tag{60}$$

however the tolerances in R and G are small compared to those in $\dot{e}$ and I_g. Hence for the sake of approximation, let

$$R - \delta R \cong R \tag{61}$$

$$G - \delta G \cong G \tag{62}$$

then Equation 49 reduces to

$$\frac{\epsilon_M}{\epsilon} \cong \frac{RGI_g(\Delta e + \delta e)}{\Delta e RG(I_g - \delta I_g)} \tag{63}$$

or $\qquad \dfrac{\epsilon_M}{\epsilon} \cong \dfrac{I_g(\Delta e + \delta e)}{\Delta e(I_g - \delta I_g)} \tag{64}$

Multiplying and dividing the numerator by Δe, and the denominator by I_g, we get that

$$\frac{\epsilon_M}{\epsilon} \cong \frac{\left[1 + \dfrac{\delta e}{\Delta e}\right]}{\left[1 - \dfrac{\delta I_g}{I_g}\right]} \tag{65}$$

From Equations 24 and 30

$$\frac{\delta e}{\Delta e} = .04$$

and
$$\frac{\delta I_g}{I_g} = .01$$

Then Equation 65 reduces to

$$\frac{\epsilon_M}{\epsilon} \cong \frac{1 + .04}{1 - .01} = \frac{1.04}{.99} \tag{66}$$

or $\quad \frac{\epsilon}{\epsilon}M \cong 1.0505) \cong 1.051$

(67)

Then from Equation 59

$$\% \text{ error } (\epsilon) \cong 100 \, (1.051 - 1) = 5.1\%$$

(68)

Appendix D

Film Reader Data

As explained in Appendix B, the force versus time curves were plotted from data by reading the oscilloscope films by means of a digital voltmeter. On the following pages, the film reader data is presented along with the corresponding force calculations for various points along the strain signal time base. The strain pulse base voltage is given for each shot, and the "base volts--film volts" column presents the difference between this value and the strain pulse voltage. The values in the Δe column were calculated from the base volts--film volts values as demonstrated in Appendix B, and the reverse load in Newtons was calculated from Equation 21. This calculation is also demonstrated in Appendix B.

Table IV

Shot #3 Film Reader Data
Base Volts = 4.564
Scope Vertical Sensitivity = 10 mv/div

Time after impact (μs)	Base volts -film volts	Δ e (mv)	Perf Force (Newtons)
1	.109	1.436	1,645
2	.362	4.769	5,465
3	.596	7.852	8,993
4	1.059	13.953	15,980
5	1.446	19.051	21,823
6	1.754	23.109	26,469
7	2.025	26.680	30,558
7.6	2.097	27.630	31,700
8	2.079	27.391	31,377
9	2.004	26.403	30,242
10	1.772	23.347	26,740
11	1.591	20.962	24,012
12	1.338	17.629	20,194
13	1.175	15.481	17,733
14	.994	13.096	15,000
15	.825	10.870	12,451
16	.825	10.870	12,451
17	.704	9.275	10,604
18	.704	9.275	10,604
19	.631	8.314	9,523
20	.614	8.090	9,264
21	.560	7.378	8,451
22	.489	6.443	7,378
23	.387	5.099	5,838
24	.326	4.295	4,922
25	.255	3.360	3,848
26	.219	2.890	3,305
27	.200	2.635	3,018
28	.144	1.900	2,173
29	.089	1.173	1,343
30	.071	.9354	1,071

Table V

Shot #4 Film Reader Data
Base Volts = 6.995
Scope Vertical Sensitivity = 5 mv/div

Time after impact (μ s)	Base volts -film volts	Δ e (mv)	Perf Force (Newtons)
1	.214	1.402	1,606
2	.724	4.744	5,434
3	1.433	9.390	10,755
4	2.120	13.893	15,913
5	2.717	17.805	20,394
6	3.186	20 878	23,914
6.4	3.258	22.553	25,832
7	3.132	20.524	23,509
8	2.753	18.040	20,661
9	1.957	12.284	14,689
10	1.846	12.097	13,857
11.4	1.523	9.980	11,432
12	1.194	7.284	8,962
13	1.031	6.756	7,736
14	.960	6.290	7,206
15	.886	5.806	6,648
16	.795	5,209	5,967
18	.588	3.764	4,311
19	.450	2.949	3,377
20	.331	2.169	2,484
21	.230	1.507	1,281
22	.140	.917	1,050
23	.085	.557	638

Table VI

Shot #5 Film Reader Data
Base Volts = 8.549
Scope Vertical Sensitivity = 5 mv/div

Time after impact (μ s)	Base volts -film volts	Δ e (mv)	Perf Force (Newtons)
1	.098	.639	732
2	.450	2.933	1,941
3	1.094	7.131	8,166
4	1.730	11.278	12,918
5	2.222	14.490	16,599
5.7	2.436	15.882	18,192
6	2.367	15.430	17,675
7	1.784	11.631	13,323
8	1.166	7.605	8,704
8.7	.692	4.513	5,166
9	.663	4.320	4,948
10	.546	3.559	4,077
11	.431	2.812	3,219
12	.382	2.490	2,852
13	.302	1.968	2,256
14	.217	2.415	1,621
15	.107	.697	798.3

Table VII

Shot #6 Film Reader Data
Base Volts = 6.910
Scope Vertical Sensitivity = 5 mv/div

Time after impact (μ s)	Base volts -film volts	Δe (mv)	Perf Force (Newtons)
2	.182	1.194	1,366
4	.345	2.264	2,594
6	.509	3.339	3,827
8	.638	4.186	4,793
10	.763	5.002	5,727
12	.890	5,840	6,688
14	.981	6.437	7,374
16	1.088	7.141	8,179
18	1.144	7.500	8,586
20	1.236	8.110	9,292
22	1.326	8.702	9,636
24	1.399	9.181	10,515
26	1.455	9.552	10,938
27	1.490	9.781	11,200
28	1.490	9.781	11,200
29	1.452	9.530	10,916
30	1.363	8.942	10,240
31	1.272	8.348	9,564
32	1.254	8.231	9,427
34	.999	6.550	7,502
36	.764	5.011	5,739
38	.528	3.463	3,963
40	.323	2.121	2,428
42	.164	1.076	1,232
44	.055	.361	413.5

Table VII

Shot #6 Film Reader Data
Base Volts = 6.910
Scope Vertical Sensitivity = 5 mv/div

Time after impact (μ s)	Base volts - film volts	Δ e (mv)	Perf Force (Newtons)
2	.182	1.194	1,366
4	.345	2.264	2,594
6	.509	3.339	3,827
8	.638	4.186	4,793
10	.763	5.002	5,727
12	.890	5,840	6,688
14	.981	6.437	7,374
16	1.088	7.141	8,179
18	1.144	7.500	8,586
20	1.236	8.110	9,292
22	1.326	8.702	9,636
24	1.399	9.181	10,515
26	1.455	9.552	10,938
27	1.490	9.781	11,200
28	1.490	9.781	11,200
29	1.452	9.530	10,916
30	1.363	8.942	10,240
31	1.272	8.348	9,564
32	1.254	8.231	9,427
34	.999	6.550	7,502
36	.764	5.011	5,739
38	.528	3.463	3,963
40	.323	2.121	2,428
42	.164	1.076	1,232
44	.055	.361	413.5

Table VIII

Shot #7 Film Reader Data
Base Volts = 3.447
Scope Vertical Sensitivity = 2 mv/div

Time after impact (μs)	Base volts - film volts	Δe (mv)	Perf Force (Newtons)
2	.165	.432	495
4	.380	.995	1,140
6	.651	1.074	1,952
8	.832	2.178	2,495
10	1.050	2.749	3,194
12	1.213	3.175	3,637
14	1.352	3.539	4,054
16	1.505	3.940	4,512
18	1.631	4.269	4,891
20	1.739	4.552	5,215
22	1.848	4.838	4,540
24	1.939	5.076	5,816
26	1.975	5.170	5,923
28	2.048	5.361	6,141
30	2.084	5.455	6,248
32	2.102	5.503	6,301
34	2.138	5.597	6,412
34.5	2.198	5.740	6,573
36	1.903	4.982	5,705
38	1.450	3.796	4,348
40	1.248	3.267	3,742
42	.855	2.238	2,563
44	.397	1.039	1,190
46	.203	.531	608
48	.075	.196	225

Table IX

Shot #8 Film Reader Data
Base Volts = 5.688
Scope Vertical Sensitivity = 2 mv/div

Time after impact (μ s)	Base volts -film volts	Δ e (mv)	Perf Force (Newtons)
.5	.054	.1494	171.1
1	.144	.398	455.9
2	.271	.750	859.1
4	.343	.949	1087
6	.452	1.250	1432
8	.542	1.499	1717
10	.648	1.793	2054
12	.688	1.903	2180
14	.742	2.053	2352
16	.787	2.177	2494
18	.822	2.274	2605
20	.840	2.324	2662
22	.877	2.426	2779
24	.906	2.506	2870
28	.938	2.595	2972
28.5	.938	2.595	2972
29	.931	2.575	2949
30	.702	1.942	2224
32	.412	1.140	1306
34	.285	.788	902.5
36	.086	.238	272.6

Table X

Shot #10 Film Reader Data
Base Volts = 6.013
Scope Vertical Sensitivity = 20 mv/div

Time after impact (μ s)	Base volts -film volts	Δ e (mv)	Perf Force (Newtons)
1	.048	1.320	1,512
2	.393	10.811	12,384
3	.737	20.275	23,225
3.7	.991	27.26	31,226
4	.942	25.91	29,677
4.5	.914	25.14	28,796
5	.756	20.80	23,825
5.7	.864	23.77	27,225
6	.828	22.78	26,095
6.3	.701	19.28	22,085
6.9	1.082	29.77	34,100
7	1.030	28.33	32,449
8	.737	20.28	23,225
9	.683	17.55	20,100
10	.628	17.28	19,794
11	.574	15.79	18,085
12	.538	14.80	16,950
13	.520	14.30	16,380
14	.465	12.79	14,649
15	.411	11.30	12,945

Table XI

Shot #18 Film Reader Data
Base Volts = 4.157
Scope Vertical Sensitivity = 10 mv/div

Time after impact (μ s)	Base volts -film volts	Δ e (mv)	Perf Force (Newtons)
.5	.184	2.480	2,840
1	.528	7.116	8,151
1.5	.885	11.927	13,662
1.8	1.089	14.677	16,811
2	1.197	16.132	18,478
2.2	1.324	17,844	20,439
2.5	1.523	20.526	23,551
3.0	1.904	25.660	29,391
3.4	1.596	21.509	24,637
3.7	1.5?3	20,526	23,511
4.0	1.361	18.342	21,009
4.5	.980	13,208	15,129
5.0	.908	12.237	14,017
6.0	.817	11.010	12,611
7.0	.419	5.647	6,499

Table XII

Shot #19 Film Reader Data
Base Volts = 6.056
Scope Vertical Sensitivity = 10 mv/div

Time after Impact (μs)	Base volts -film volts	Δe (mv)	Perf Force (Newtons)
1	.635	8.758	9,928
1.8	1.288	14.77	20,350
2	1.414	19.50	22,335
2.8	1.993	27.49	31,488
3.0	1.921	26.50	30,353
4.0	1.396	19.26	22,054
4.7	1.107	15.27	17,493
5.0	1.123	15.49	17,742
6.0	.995	13.72	15,717
7.0	.871	12.01	13,755
8.0	.798	11.01	12,611
9.0	.690	9.517	10,903
10	.673	9.283	10,631
11	.563	7.766	8,889
12	.491	6.772	7,756
13	.491	6.772	7,756
14	.436	6.014	6,889
15	.373	5.145	5,892
16	.309	4.262	4,882
17	.163	2.248	2,575
18	.109	1.503	1,722
19	.061	.841	963

Table XIII

Shot #20 Film Reader Data
Base Volts = 4.531
Scope Vertical Sensitivity = 5 mv/div

Time after impact (μ s)	Base volts - film volts	Δ e (mv)	Perf Force (Newtons)
.8	.813	5.622	6,493
1	1.066	7.372	8,446
1.6	1.573	10.880	12,460
1.9	1.609	11.130	12,749
2.0	1.645	11.380	13,034
2.3	2.296	15.880	18,183
2.6	2.405	16.632	19,050
3.0	1.880	13.000	14,890
3.2	1.641	11.350	12,998
3.6	1.627	11.250	12,887
4.0	1.048	7.247	8,299
5.0	.812	5.615	6,430
6.0	.613	4.239	4,855
7.0	.541	3.741	4,285
8.0	.397	2.746	3,145
9.0	.387	2.674	3,065
10.0	.252	1.743	1,996
11.0	.157	1.086	1,244

Table XIV

Shot #21 Film Reader Data
Base Volts = 4.732
Scope Vertical Sensitivity = 20 mv/div

Time after impact (μ s)	Base volts -film volts	Δe (mv)	Perf Force (Newtons)
.25	.579	16.017	18,346
.48	.697	19.281	22,085
.75	.822	22.739	26,046
1.0	1.012	27.994	32,065
1.25	1.103	30.512	34,949
1.70	1.374	38.008	43,536
1.90	1.498	41.438	47,464
2.0	1.628	45.035	51,584
2.4	2.008	55.546	63,626
2.75	1.754	48.520	55,576
3.0	1.664	46.030	52,724
3.3	1.410	39.004	44,678
3.75	1.356	37.510	42,965
4.0	1.212	33.527	38,404
5.0	1.067	29.515	33,807
5.5	.669	18.506	21,195
6.1	.559	15.463	17,711
7.0	.434	12.006	13,751

Table XV

Shot #22 Film Reader Data
Base Volts = 6.114
Scope Vertical Sensitivity = 20 mv/div

Time after impact (μs)	Base volts -film volts	Δ e (mv)	Perf Force (Newtons)
.4	.676	18.44	20,902
.8	.784	21.39	24,502
1.05	.966	26.36	30,193
1.4	.821	22.40	.5 ,54
1.9	1.292	35.25	4u, 75
2.05	1.382	37.71	43,196
2.7	1.831	49.96	57,227
3.0	1.307	35.66	40,847
3.3	.803	21.91	25,094

Table XVI

Shot #23 Film Reader Data
Base Volts = 6.710
Scope Vertical Sensitivity = 20 mv/div

Time after impact (μ s)	Base volts - film volts	Δ e (mv)	Perf Force (Newtons)
.15	.634	17.346	33,241
.3	1.163	31.819	36,445
.5	1.743	47.688	54,544
.65	2.069	56.607	64,841
.9	1.978	54.177	62,055
1.2	2.338	63.967	73,269
2	.998	27.305	31,275

Table XVII

Shot #24 Film Reader Data
Base Volts = 5.674
Scope Vertical Sensitivity = 20 mv/div

Time after impact (μ s)	Base volts -film volts	Δ e (mv)	Perf Force (Newtons)
.59	.671	18.484	21,173
.7	.761	20.964	23,994
1.3	1.086	29.917	34,265
1.55	.942	25.950	29,721
2.05	1.467	40.413	46,289
2.75	1.918	52.837	60,520
3.2	1.304	35.922	41,146
3.6	.943	25.977	29,753

Vita

Visi Arajs was born on ███████ in Madona District, The Republic of Latvia. At this time the country was in a period of transition from Soviet to German occupation as a result of World War II.

In 1944, he and his family moved to Germany to escape the advancing eastern front, and at the end of World War II, settled in a displaced person's camp in the American zone of occupation.

He and his family immigrated to the United States in January of 1950, where they established a home in Santa Rosa, California. He graduated from high school in 1960 and attended Santa Rosa Junior College before enlisting in the Air Force in 1963. A year later he was selected for the Airman's Education and Commissioning Program through which he earned a Bachelor of Science degree in aerospace engineering from Auburn University in Alabama.

Upon completion of officer training school, he was assigned to the Space and Missile Systems Organization of the Air Force Systems Command at Norton AFB, California. Prior to his selection for graduate training in 1969, he was responsible for monitoring structural component and assembly procedure development for the Minuteman III ICBM. He is a member of the Sigma Gamma Tau scholarship fraternity.

This thesis was typed by Mrs. Cynthia A. Dapore